TITLE

A CRISPR toolbox for generating intersectional genetic mice for functional, molecular, and anatomical circuit mapping

AUTHOR NAMES AND AFFILIATIONS

Savannah J. Lusk[1], Andrew McKinney[1], Patrick J. Hunt[3], Paul G. Fahey[1], Jay Patel[1], Jenny J. Sun[1], Vena K. Martinez[2], Ping Jun Zhu[1], Jeremy R. Egbert[4], Xiaolong Jiang[1], Benjamin R. Arenkiel[3,5], Andreas S. Tolias[1], Mauro Costa-Mattioli[1], Russell S. Ray[1,5,6]

[1]Department of Neuroscience, Baylor College of Medicine, Houston TX

[2]Department of Pharmacology, Baylor College of Medicine, Houston TX

[3]Department of Molecular and Human Genetics, Baylor College of Medicine, Houston TX

[4]Department of Cell Biology, University of Connecticut, Farmington CT

[5]McNair Medical Institute, Houston Tx

[6]Corresponding author, russell.ray@bcm.edu

ABSTRACT

Background

A full understanding of circuits and cellular mechanisms governing health and disease requires the dissection and multi-faceted study of discrete cell subtypes in developing and adult animal models. Recombinase-driven expression of transgenic response alleles represents a significant and powerful approach to delineate cell populations for functional, molecular, and anatomical study. In addition to single recombinase systems, the expression of two recombinases in distinct, but partially overlapping, populations allows for more defined target expression. Although the application of this method is becoming increasingly popular, the expense and difficulty associated with production of customized intersectional mouse lines have limited widespread application to more common allele manipulations that are often commercially produced at great expense.

Results

We present a simplified CRISPR toolkit for rapid, inexpensive, and facile intersectional allele production. Briefly, we produced 7 intersectional mouse lines using a dual recombinase system, one mouse line with a single recombinase system, and three embryonic stem (ES) cell lines that are designed to study how functional, molecular, and anatomical features relate to each other in building circuits that underlie physiology and behavior. As a proof-of-principle, we applied three of these lines to different neuronal populations for anatomical mapping and functional *in vivo* investigation of respiratory control. We also generated a mouse line with a single recombinase-responsive allele that controls the expression of the calcium sensor Twitch-2B. This mouse line was applied globally to study the effects of follicle stimulating hormone (FSH) and luteinizing hormone (LH) on calcium release in the ovarian follicle.

Conclusions

Lines presented here are representative examples of outcomes possible with the successful application of our genetic toolkit for the facile development of diverse, modifiable animal models. This toolkit will allow labs to create single or dual recombinase effector lines easily for any cell

population or subpopulation of interest when paired with the appropriate Cre and FLP recombinase mouse lines or viral vectors. We have made our tools and derivative intersectional mouse and ES cell lines openly available for non-commercial use through publicly curated repositories for plasmid DNA, ES cells, and transgenic mouse lines.

KEY WORDS

Intersectional genetics, mouse models, CRISPR toolkit

BACKGROUND

Targeted expression of effector molecules, like fluorescent markers, calcium reporters, optogenetic actuators, or exogenous ligand-responsive receptors (DREADDs) (1), are increasingly applied in a variety of fields for greater precision, quantitative expression level control, and reduced side effects compared to previous methods for labeling and manipulation. For example, the Cre/LoxP system is used to achieve permanent cell-type restriction by using a promoter or enhancer to express the site-specific recombinase Cre (2). In such examples, cre transgenes are paired with a constitutively active, but conditional, allele where expression of an effector molecule, such as eGFP, is interrupted by a LoxP-Stop-LoxP cassette that is recombined out by Cre, which enables expression in targeted, Cre-expressing cells. The use of various effector molecules in this paradigm enables fluorescent marking, neuronal perturbation, molecular affinity pull-downs, activity tracking, and other studies (1,3–28).

In some fields, it is becoming increasingly clear that recombinase expression based on a single gene does not offer the resolution needed for a variety of developmental or targeting applications, like circuit mapping (29–31). Intersectional genetics adds needed resolution by employing a dual recombinase system using both Cre recombinase as well as a second recombinase, FLP, to activate a conditional effector allele only in cells where both recombinases have been expressed in the same cell (though not necessarily concurrently) (20,32–39). With new methodologies being developed to use Cre and FLP not only as traditional genetic markers, but also as activity and connectivity markers, unique combinatorial cell type definitions become possible (40–44). Thus, a resource consisting of multiple dual recombinase intersectional alleles that each express different effector molecules would add significant value and needed resolution to our ability to deconstruct neural circuits on multiple levels. This technology could also be applied to a multitude of other fields where intersectionally defined subpopulations of target cells exist and may play different roles in the measured outcomes.

73 Although mouse intersectional technology provides relatively benign access to otherwise
74 inaccessible populations of cells, few laboratories have generated single transgenic or
75 intersectional genetic mouse lines in house for a number of reasons. The complexity and size of
76 the final targeting vectors puts them beyond present (cost-effective) commercial DNA synthesis
77 capabilities, thus requiring some level of recombinant DNA cloning and precluding straightforward
78 production of large, high fidelity ssDNA donors that can facilitate pro-nuclear CRISPR-mediated
79 targeting (45). While intersectional targeting vectors are available from the Addgene plasmid
80 repository, they are finished vectors that require significant reverse engineering or modifications
81 for use in a new context or approach. To our knowledge, there are no modular intersectional
82 targeting vectors that are publicly available for facile and rapid production of new targeting alleles
83 for the generation of intersectional mouse models. Furthermore, vector stability and other *in vitro*
84 difficulties combined with the expense and time associated with target vector insertion and mouse
85 line production limit the number of intersectional mouse lines available for public use. Thus, the
86 production of intersectional genetic mouse lines has been largely limited to a small number of
87 pioneering labs or resource rich institutions such as the Howard Hughes Medical Institute and the
88 Allen Institute for Brain Science (38,46).

89 To address these pitfalls and make the production of intersectional genetic mouse models more
90 widely feasible, we aimed to produce a freely available resource toolbox consisting of several
91 intersectional and single-recombinase responsive *Rosa26* targeting vectors for rapid, facile, and
92 cost-effective generation of complex mouse lines through the use of CRISPR/Cas9-mediated
93 homologous recombination in mouse embryonic stem cells and early oocytes. In oocytes,
94 genomic insertions/deletions (in/dels) and short targeted insertions are readily produced whereas
95 large construct targeting in oocytes has shown more limited but growing success. Additionally,
96 requisite equipment and facilities are difficult to access and out of reach for many investigators.
97 ES cell approaches are well established and widely available, allowing for rapid screening and

98 identification, and, if using morula aggregation, require much simpler methodologies and
99 equipment for mouse generation.

100 Towards this, we produced 7 intersectional mouse lines using a dual recombinase system; one
101 mouse line with a single recombinase system, and three additional ES cell lines to study how
102 functional, molecular, and anatomical features relate to each other in building the circuits that
103 underlie physiology and behavior. As a proof-of-principle, we applied three of these lines to
104 different neuronal populations for anatomical mapping and functional *in vivo* characterization in
105 respiratory control. Next, we globally applied the single recombinase-responsive line, which
106 controls the expression of the calcium sensor Twitch-2B. Twitch-2B was expressed globally in the
107 generated mouse line to study the effects of follicle stimulating hormone (FSH) and luteinizing
108 hormone (LH) on calcium release in the ovarian follicle. The publication and availability of this
109 technology will allow for the seamless production of a highly diverse group of mouse lines that
110 can be used to generate animal models of human disease, label specific cell populations for
111 developmental or connectivity studies, or modulate cellular activity in established disease model
112 lines, among other possibilities. All reagents and vectors used or generated in this study are now
113 openly available for not-for-profit research.

114 **RESULTS**

115 **Vector design and optimization:** For each of the targeting vectors generated, the intersectional
116 or Dre-responsive cassette was knocked into a well-established site in the *Rosa26* locus (**Fig. 1)**
117 (47,48). For positive ES cell clone selection, the targeting vector was simplified and improved in
118 several ways compared to earlier approaches (49). A simplified neomycin resistance cassette
119 was integrated into the intersectional cassette before the second LoxP-flanked stop cassette to
120 utilize the *CAG* promoter and polyadenylation (*pA*) sequences of the FRT flanked stop cassette
121 eliminating prior use of an additional PGK promoter and *Bovine Growth Hormone polyA* (BGHpA*)*
122 signal. To use CRISPR/Cas9, we cloned an sgRNA that was close to the 5'/3' homology junction
123 into the px330 vector (50), which expresses both Cas9 and the subcloned sgRNA
124 (*px330_Rosa26_sgRNA*). A Woodchuck Hepatitis Virus (WHV) Posttranscriptional Regulatory
125 Element (WPRE) and BGHpA were added at the end of the expression cassette to enhance
126 effector molecule expression and limit reliance on the disrupted Rosa Locus for transcript
127 termination (49). The homology arms were significantly shortened to 1Kb to remove repetitive
128 genomic sequences and stabilize the vector for prokaryotic propagation. Lastly, the terminal non-
129 homology Diphtheria Toxin A (DTA) chain negative selection cassette was removed, allowing for
130 the complete targeting vector to be functionally tested via cell culture or *in utero* electroporation,
131 which was not possible with the presence of the terminal DTA selection cassette without an
132 additional subcloning step. Redesigned vectors and their Addgene ID numbers are outlined in
133 Table 1 for public distribution.

134 **Embryonic stem cell electroporation:** We optimized traditional but widespread ES cell targeting
135 by applying CRISPR/Cas9-mediated HDR (51). Our initial electroporation (EP) experiments using
136 an earlier, more complex version of the *Rosa26* intersectional targeting vector (containing the
137 longer 4.2 kb 3' homology arm, DTA, and no CRISPR/Cas9) showed targeting rates ranging from
138 6-14% (over the course of four electroporations we saw targeting rates of 6/48, 3/48, 7/48, and

139 3/48 clones, mouse strains listed in **Table 2**). To determine the effect of CRISPR/Cas9 on
140 targeting efficiency, we co-electroporated the *px330_Rosa26_sgRNA* vector expressing Cas9
141 and a *Rosa26* specific sgRNA with the optimized *RR5* targeting vector at four different molar
142 ratios (0:1, 0.5:1, 1:1, and 10:1), proportionally decreasing the amount of donor vector to
143 accommodate the increasing *px330_Rosa26_sgRNA* vector per EP (18-20µg total DNA per EP
144 for $1x10^7$ ES cells) (**Fig 1C)**. Under the 0:1 *px330* vector:donor vector condition, we saw a 6%
145 targeting rate similar to those seen in electroporations without Cas9 and with a much longer 3'
146 homology arm and negative selection, suggesting that the shortening did not have a large impact
147 on targeting efficiency under our EP conditions. Under the 0.5:1, 1:1, and 10:1 conditions, we
148 observed 33%, 27%, and 58% targeting, respectively, suggesting that higher ratios of the Cas9
149 vector resulted in increased targeting efficiency (**Fig. 1D)**.

150 Since the 10:1 ratio had the highest targeting efficiency, despite significantly less donor DNA, we
151 used this ratio in subsequent EPs. Because the targeting efficiency was notably high, we next
152 attempted a single electroporation with multiple vectors targeting the same locus, but containing
153 equimolar amounts of five different cassettes, while keeping the overall *px330_Rosa26_sgRNA*
154 vector to total donor vector ratio at 10:1. The five vectors consisted of: 1) a Cre/FLP responsive
155 mutant methionyl-tRNA synthetase (*RR6*) for selective labeling of newly synthesized proteins; 2)
156 a Cre/FLP responsive modified G-protein coupled receptor (*RR7*); 3) a Cre/FLP responsive
157 bicistronic reporter with H2B-TagBFP and sfGFP separated by a p2a element, and tdTomato
158 expressed in the subtractive population (cells that express FLP but not Cre) (*RR9*); 4) a Dre-
159 responsive tricistronic reporter with H2B-TagBFP, sfGFP, and synaptophysin-tdTomato
160 separated by p2a elements (*RR11*); and 5) a Dre-responsive bicistronic reporter with H2B-
161 TagBFP and sfGFP separated by a p2a element (*RR10*). We saw a 52% targeting efficiency and
162 successful targeting of all five cassettes at varying efficiencies (**Table 3**). Due to the lower
163 targeting efficiency of *RR7* (2%), we attempted another 10:1 electroporation using the *RR7* donor

164 vector alone and obtained a 63% targeting efficiency (genotyping results shown in **Fig. 1**). Thus,
165 our results show that we are able to target and recover as many as five *Rosa* alleles in a single
166 EP, significantly increasing efficiency and reducing costs toward intersectional mouse generation.

167 **Oocyte targeting:** Given the high efficiency of targeting, we also attempted to create a founder
168 line (*RR8*) through direct oocyte injection of the optimized *Rosa26* targeting vector with a Cre-
169 responsive calcium indicator, Twitch (52) (total cassette size without homology arms, 6.5kb),
170 using pro-nuclear injection of Cas9 protein (30 ng/µl), sgRNA (20 ng/µl), and double-stranded
171 DNA plasmid (2 ng/µl). A total of 1266 embryos were injected yielding 129 mice, of which 7
172 genotyped positive for the calcium indicator but only one targeted successfully (<1% targeting
173 efficiency of mice born), suggesting that direct oocyte injection is inefficient with this system under
174 the specified parameters.

175 **Off-target analysis:** Genomic sequences that are similar to the sgRNA used for targeted double
176 stranded breaks may cause unintended gene mutations or editing at off-target sites. To account
177 for this possibility, we predicted the off-target sites for each sgRNA using the crispr.mit.edu tool
178 and selected the top 5 sites for follow up. We PCR amplified and sequenced these loci from three
179 correctly targeted ES cell clones and did not detect any genetic changes (**Fig. 2**). While we cannot
180 rule out off-target effects in other loci, these data suggest that off-target effects are not prevalent
181 in this setting.

182 **Mouse line derivation:** The goal of our efforts was to produce freely available genetic tools that
183 delineate and access distinct populations for multi-faceted circuit mapping or functional
184 characterization studies. With this toolkit in hand, we collectively produced 11 intersectional or
185 Dre-responsive alleles available as either mouse lines (8) or ES cells (3) **(Table 2)**. To perturb
186 neuron function, we produced three lines that express metabotropic DREADD receptors, hM4D
187 (*RR1*), hM3D (*RR2*), and Rs-EGFP (*RR7*), and a fourth line expressing the ionotropic PSAM

188 receptor (*RR4*) (24,53,54). Two lines enable molecular characterization: one expresses the
189 EGFP-L10A fusion protein for ribosomal affinity purification and capture of translating mRNAs
190 (*RR3*) (55), while the second line expresses methionyl-tRNA synthetase (Met-RS) that
191 incorporates an artificial amino acid into nascent peptides (*RR6*) (13). One line enables ratiometric
192 calcium imaging via expression of Twitch2B (*RR8*). Our neuro-anatomical mapping lines
193 described below also incorporate a tagged histone (H2B), offering the possibility of chromatin
194 affinity isolations. We created four alleles of differing Cre, FLP, and Dre recombinase responsive
195 configurations that fluorescently mark distinct cellular compartments for unambiguous cell counts,
196 morphological characterizations, and projection mapping (*RR5, RR9, RR10, RR11)*. The
197 derivation of lines *RR5*, *RR6*, and *RR7* demonstrated that ES pluripotency was maintained, and
198 that germline transmission was not diminished in our Cas9-mediated single and multiplexed
199 electroporations after correctly targeted clones were selected and injected into blastocysts for
200 chimera generation.

201 **Select mouse line characterization:** Upon dual recombinase expression, the *RR5* tricistronic
202 multi-color reporter allele expresses three spectrally separated and modified fluorescent proteins
203 to highlight the nucleus in blue, fill the neuron in green, and emphasize pre-synaptic contacts in
204 red. At the site of dual recombinase expression, targeted cells brightly label with TagBFP, sfGFP,
205 and tdTomato where TagBFP fluorescence is constrained to the nucleus by an H2B fusion, sfGFP
206 is unmodified so that fluorescence is seen throughout the cell body, and tdTomato is fused to
207 synaptophysin (56) so that fluorescence is excluded from nuclear areas and primarily seen in
208 projection areas. Individual nuclei can be resolved using blue fluorescence and co-localization
209 with sfGFP-labeled somata.

210 We used *RR5* to evaluate the functional activity and specificity *in vivo* of our CRISPR/Cas9
211 approach to generating mouse lines in three distinct contexts; 1) germline recombinase
212 expression, 2) viral recombinase expression, and 3) combinatorial retrograde viral and germline

213 recombinase expression to target single gene defined neurons by a specific projection field. First,
214 to demonstrate genetically-restricted, germline expression of recombinases in the intersectional
215 *RR5* line, we bred the *RR5* line to a double *Dopamine-Beta-Hydroxylase (DBH)*^{p2aFLPo}(51); *Bactin-*
216 *Cre* recombinase driver to express the tricistronic fluorescent cassette in *DBH*-positive
217 noradrenergic neurons in the brainstem **(Fig. 3 A-H)**. In both the locus coeruleus (**Fig. 3 A-D)** and
218 the A5 nucleus (**Fig. 3 E-H)** as well as all other noradrenergic nuclei (not shown), we could cleanly
219 resolve blue nuclei, green cells, and red puncta without the need for antibody enhancement.
220 Additionally, we bred an intersection of double *Vgat-Cre; Vglut2-FLPo* recombinase expression
221 to the *RR5* line and found the entopeduncular nucleus labeled green with local projections labeled
222 red and distal projections in the lateral habenula labeled red (DAPI was applied to help delineate
223 the target field, obscuring the genetic TagBFP signal) (**Fig. 3 J-K**).

224 Second, we verified viral expression of Cre and FLP recombinase where adult *RR5* mice were
225 stereotaxically injected with equal titer amounts of AAV viruses expressing Cre and FLP into the
226 dentate gyrus **(Fig. 4 A-H)**, amygdala (**Fig. 4 I-P**), and olfactory bulb (**Fig. 4 Q-T**). Clear
227 expression of all three fluorescent proteins were resolved at the site of injection to the appropriate
228 cellular locations. Third, defining properties of the subpopulations can be extended to include any
229 combination of gene expression or anatomical location and projection target when injection of
230 retrograde viral vectors is applied. To utilize this option, we genetically marked a neuronal subtype
231 defined by the partial overlap of a genetic selector and projection target by injecting canine
232 adenovirus 2 (CAV2)-Cre virus (57,58) into the basolateral amygdala of *DBH*^{p2aFLPo}*; RR5* mice
233 that express only FLP in all noradrenergic neurons. CAV2-Cre virus efficiently transduces axon
234 terminals, thus genetically marking presynaptic neurons. In this context, only noradrenergic
235 neurons expressing DBH that project to the amygdala express both Cre and FLP and the resulting
236 tricistronic fluorescent cassette (**Fig. 5 A)**. We only observed recombination in the brainstem
237 noradrenergic nuclei and in the locus coeruleus, primarily on the ipsilateral side (**Fig. 5 B-E**) with

238 some sparse marking on the contralateral side (**Fig. 5 F-I**), in agreement with a prior study (59).
239 Overlapping red and green puncta (with no blue) could be seen in the injected amygdala,
240 suggesting that the marked neurons project to the amygdala, as expected given the nature of the
241 CAV2-Cre virus (**Fig. 5 J-M).** We also observed collateral projections to several additional areas
242 in the mid and forebrain, including the dorsal raphé (**Fig. 5 N-Q)**, reticulotegmental pontine nuclei
243 **(Fig. 5 R-U)**, dentate gyrus **(Fig. 5 V-Y)**, and olfactory bulb (**Fig. 5 Z-CC).** This restriction by
244 retrograde selection was also achieved in other regions of the brain with a second viral vector.
245 *Vglut2_Cre; RR5* mice were injected with retro-AAV-Ef1a-FLPo into the lateral hypothalamus
246 (**Fig. 6 A**) where tricistronic expression was clearly visualized in the cingulate gyrus (**Fig. 6 B-E**),
247 piriform cortex (**Fig. 6 F-**I), and medial habenula (**Fig. 6 J-M**), indicating these regions as pre-
248 synaptic inputs to the lateral hypothalamus. Together, these results are in agreeance with
249 previous connectivity studies (59).

250 Before *in vivo* characterization of the cell autonomous DREADD systems coded by *RR1* and *RR2*,
251 we first examined the ability of the *RR1 and RR2* lines to modulate *Tg(Dbh-cre)KH212Gsat*
252 *(TgDBH-Cre)*-defined NA neuron activity at the cellular level. We conducted whole-cell recordings
253 from P30-P60 locus coeruleus neurons from Cre-only responsive alleles of mouse lines. These
254 lines were developed by germline deletion of the FRT flanked stop cassettes by crossing to the
255 *Bact_FLPe* allele(60) (*RR1P, RR2P)* or using the previously published *RC::FPDi* (*RC::PDi),* each
256 bred to the *RC::FrePe*(61) (also previously bred to the *Bact_FLPe* mouse line to produce the Cre
257 only responsive *RC::epe)* line to express both GFP and a DREADD in *TgDBH-Cre*-defined cells
258 for acute brain slice visualization of DREADD expressing neurons. *RC::PDi*(49) was included as
259 it represents a similarly constructed hM4D intersectional allele, but lacks the modifications and
260 optimizations made in our targeting system (**Fig. 1 A**). For example*, RC::PDi* contains an
261 additional PGK Promoter and pA signal sequence flanking neomycin in the first stop cassette and
262 lacks the WPRE element and pA found in *RR1* and *RR2*. We hypothesized that the addition of a

263 Woodchuck Hepatitis Virus (WHV) Posttranscriptional Regulatory Element (WPRE) would
264 enhance DREADD effectiveness. After bath application of 10 μM CNO, for *RR2P; RC::epe* we
265 observed a change in depolarization from pre-CNO average = -62.26±1.53 to a post-CNO
266 average = -55.09±2.16 mV (p = 0.0034) (n=19 neurons across 3 mice). After bath application of
267 10 μM CNO, for *RR1P; RC::epe* we observed a change in hyperpolarization from pre-CNO
268 average = -56.98±3.50 mV to post-CNO average = -65.3137±3.60 mV (p = 0.046) (n=10 neurons
269 across 3 mice). After bath application of 10 μM CNO, for *RC::PDi; RC::epe* we observed a change
270 in hyperpolarization from pre-CNO average = -53.71±2.93 mV to post-CNO average = -
271 56.72±3.42 mV (p = 0.027) (n=10 neurons across 3 mice) (**Fig. 7 A-C**).

272 We net performed whole-body plethysmography to assess changes in respiratory function caused
273 by CNO-DREADD mediated perturbation of targeted neurons *in vivo*. *DBH-Cre* defined NA
274 neurons were inhibited by crossing mouse line *RR1P* to *Tg(Dbh-cre)KH212Gsat (TgDBH-Cre)*
275 mice. We observed no changes under room air conditions (**Fig. 8 A)**. However, under hypercapnic
276 conditions, we saw a reduction in ventilation (**Fig. 8 B)**, with decreases in V_T (-26.6%, p=0.0021,
277 **Fig. 8 D**), $\dot{V}_E$ (-26.8%, p=0.026, **Fig. 8 E**), and $\dot{V}_E/\dot{V}_{O2}$ (-28.7%, p<0.0001, **Fig. 8 G**). No significant
278 differences were observed in body temperature between experimental animals and sibling
279 controls (**Fig. 8 H**). Notably, sibling controls showed no difference in respiratory parameters pre-
280 and post-CNO administration.

281 We then tested the applicability of the *RR2P* line *in vivo.* After CNO-DREADD mediated
282 stimulation of *DBH-Cre* defined neurons, we saw significant increases under room air ventilation
283 (**Fig. 9 B)** in V_f (+28.1%, p=0.0076, **Fig. 9 D**), V_T (+43.3%, p=0.00077, **Fig. 9 E**), $\dot{V}_E$ (+83.6%,
284 p<0.0001, **Fig. 9 F**), and $\dot{V}_{O2}$ (+50.9%, p<0.0001, **Fig. 9 G**). The increase in $\dot{V}_E$ was proportional
285 to the increase in $\dot{V}_{O2}$, however, so $\dot{V}_E/\dot{V}_{O2}$ remained constant **(Fig. 9 H)**. Under hypercapnic
286 conditions, as compared to pre-CNO values, $\dot{V}_{O2}$ was increased (+37.2%, p=0.0015, **Fig. 9 G)**,

287 resulting in a reduced $\dot{V}_E/\dot{V}_{O2}$ (-24.2%, p=0.04, **Fig. 9 H)**. We also observed a deficit in body
288 temperature in *DBH-Cre; RR2P* animals 30 minutes after the end of the assay at room
289 temperature (~1.5 hrs after CNO injection) as compared to sibling controls (**Fig. 9 I)**, but not
290 immediately at exit from the respiratory chamber, which is kept at a thermoneutral temperature,
291 30-32°C**.** Sibling controls showed no difference in respiratory parameters pre- or post-CNO
292 administration. The respiratory phenotypes seen here clearly demonstrate an acute and cell
293 autonomous involvement of the whole NA system in CO_2 chemosensitivity and baseline
294 metabolism while avoiding the confounds of developmental compensatory events or off-target
295 effects. Collectively, these data highlight how our intersectional lines can be used to functionally
296 assess dispersed and difficult to access neuronal populations, setting the stage for further
297 characterization and dissection of a variety of neuronal systems in a given measured outcome
298 through intersectional subdivision by genetic or viral methods.

299 Finally, we characterized a fourth line, produced by oocyte CRISPR-mediated recombination to
300 express the Twitch2B ratiometric calcium indicator upon Cre recombinase expression. Calcium
301 signaling was recorded in outer granulosa cells surrounding an oocyte taken from a germline
302 recombined (*RR8; Bact_Cre*) mouse line (**Fig. 10 A**). Upon application of 10μM ionomycin in the
303 presence of 10mM $CaCl_2$, the YFP/CFP ratio increased more than 3-fold (**Fig. 10 B**). The data
304 demonstrate how the targeting system here can be used to build conditional mouse lines that are
305 useful beyond the nervous system and throughout the body (62).

306 **DISCUSSION**

307 **Vector design and optimization:** Our tricistronic mouse line vector (*RR5*) was a complex vector
308 to design. Thus, the discussion of its construction applies to the other simpler vectors and best
309 describes choices made to optimize the vectors. Our initial goal was to create an intersectional
310 mouse strain expressing three fluorescent components to highlight the nucleus, whole neuron,
311 and presynaptic contacts, enabling facile study of cell counts, cellular morphology, and axonal
312 and projection targets (*RR5* consisting of H2B-TagBFP, sfGFP, and synaptophysin-tdTomato
313 separated by p2a elements) without the need for signal amplification using antibodies. However,
314 likely due to the high number of repetitive elements in the *Rosa26* 3' homology arm and the high
315 complexity and repetitive components of the intersectional cassette (i.e. two stop cassettes
316 consisting of multiple SV40 polyadenylation sequences, tdTomato protein dimer, double loxP and
317 FRT sites, and two p2a self-cleaving peptides separating the elements), we had no success in
318 stably subcloning the intersectional cassette into a low copy vector (p15a ori) containing the
319 original *Rosa26* homology arms (1.1kb 5' homology arm and 4.2 kb 3' homology arm) and DTA
320 negative selection gene (49). Thus, we sought to make a number of improvements on the prior
321 approaches used to build intersectional genetic mice. First, we sought to stabilize the vector by
322 shortening the homology arms and eliminating repetitive genomic elements found at the *Rosa26*
323 locus. Second, we removed the DTA negative selection terminal non-homology to eliminate the
324 need to validate intersectional cassettes separately before placing the cassette in the targeting
325 vector. Third, we reduced the size of the selection cassette. Prior intersectional constructs carried
326 an additional PGK promoter and BGHpA tail for neomycin expression. We eliminated both
327 promoter and BGHpA as the functions of these elements can easily be served by the CAG
328 promoter and SV40pA in the stop cassette. With smaller homology arms, it was possible that our
329 targeting efficiency would fall. Therefore, we introduced a CRISPR/Cas9 targeting strategy to
330 enhance homologous recombination in either ES cells or oocytes. Surprisingly, in ES cells, the

331 shorter homology arms performed equally well as the full-length homology arms (see discussion
332 below). The resulting strategy offered a simplified, smaller, and highly stable vector that remains
333 efficient at targeting the *Rosa26* locus. Through this optimization process we built a set of baseline
334 vectors that can be used to rapidly and inexpensively build any intersectional genetic targeting
335 allele by simply cloning in a cDNA of interest into one or both of the multiple cloning sites for both
336 intersectional and subtractive expression.

337 **Embryonic stem cell electroporation:** While CRISPR strategies are widespread for knockout
338 mutations and small deletions and insertions in mouse zygotes, consistent knock-in of large
339 targeting cassettes (>4kb) still remains a challenge with fewer but increasing successes (63–65).
340 To address this limitation, our new multiplexed methodology enabled us to: **1)** simplify our base
341 targeting vector to less than 5kb in total length; **2)** see successful targeting of added cassettes up
342 to 11kb; **3)** increase the rate of targeting by 5-10 fold over previous *Rosa26* targeting attempts
343 (that used a significantly longer 3' homology arm) under our ES cell strain and conditions; and **4)**
344 further reduce cost by co-electroporating five different targeting vectors in a single ES cell
345 electroporation that were easily resolved to produce new mouse lines. While targeting rates for
346 the *Rosa26* locus can vary greatly in the literature, we compare only to our own experiments, as
347 significant variability in targeting efficiency from lab to lab or facility to facility can arise from the
348 several factors in ES cell electroporation ranging from electroporation conditions (e.g. buffer ionic
349 strength, adjuvants, field strength, field duration, field shape, square wave vs exponential decay,
350 etc.) to culture conditions (ES cell strain and genetic background, feeder type, media composition,
351 inclusion of LIF, etc.). Notably, when we co-electroporated a CRISPR/Cas9 plasmid to facilitate
352 targeting, there was a proportional increase in targeting efficiency despite reduced amounts of
353 targeting vector (total DNA in the EP was capped at 18-20 μg per EP). At the highest efficiencies,
354 we could further subdivide the small amount of targeting vector across multiple plasmids, which
355 allowed us to introduce and recover as many as five vectors in a single EP. This multiplexed

356 approach significantly reduced the costs of mouse production via ES cells. With these goals met,
357 multiplexed ES cell targeting enables the rapid and high throughput production of intersectional
358 alleles that can be readily distributed throughout the mouse research community for further
359 studies.

360 **Oocyte targeting:** Oocyte injection was only attempted with one line, *RR8*. Less than 1% of the
361 embryos contained a properly targeted vector, which in our experience suggests that direct oocyte
362 injection is not efficient. Future optimization and the development of new technologies may
363 increase the efficiency of targeting for more rapid generation of transgenic mice; for example, a
364 study showed 10-20% targeting of 8-11kb cassettes to the *Rosa26* locus in oocytes using longer
365 homology arms, while another showed successful targeting of a 5.5kb cassette into the *Rosa26*
366 locus in rats with co-injection of two ssDNA oligos (65,66). As noted above, there can be
367 significant variability in targeting across labs based upon a variety of factors including background
368 strain (vs strain from which the homology arms are derived), the use of Cas9 mRNA or protein,
369 and site of injection (pro-nucleus vs cytoplasm, single vs 2-cell stage). Thus, our outcomes here
370 may reflect our core facility capabilities as much as inherent limitations in consistent Cas9
371 mediated oocyte targeting of large constructs. The successful outcomes here and in a prior
372 publication demonstrate the use of the system to develop lines capable of functional imaging (62).

373 **Select mouse line characterization:** Intersectional expression of fluorescent proteins (FPs) has
374 been used to great effect for anatomical characterizations of targeted neuron populations (61,67).
375 Characterizations aimed at counting or highlighting single cells or cell populations made with a
376 single FP can be made difficult, however, in cases where cell, axon, or dendrite density (neuropil)
377 is high. Usually, one or two FPs are deployed to either fill the cell or highlight specific features,
378 which necessitates the use of multiple reporter alleles to clearly observe cell number, morphology,
379 and projections. To ameliorate these issues, we sought to create a mouse line (*RR5*) that
380 highlights three specific features in an intersectionally defined neuron. Overall, this novel three-

381 color mouse line enables intersectional and simultaneous labeling of three subcellular
382 compartments. The polycistronic fluorescent labeling cassette gives unambiguous cell counts and
383 clear visualization of cell morphology, axonal projections, and synaptic contacts. The strength of
384 expression of all three colors is likely due to the use of p2a elements, rather than IRES elements,
385 which cause expression level reduction. Reduced expression from an IRES may stem from cryptic
386 splice elements in the IRES that could interact with the intron in the CAG promoter or splice
387 acceptors in some stop cassettes (68). Our use of P2A appears to bypass those issues as all
388 three fluorescent proteins could be readily visualized without additional enhancement as
389 compared to other approaches (35).

390 We also show that combinations of germline, viral, and retrograde viral expression of
391 recombinases in the *RR5* line can all be used to clearly map the shared innervation of multiple
392 regions by a small subset of genetic, projection, and/ or intersectionally defined neurons. In
393 contrast to prior intersectional studies using two genetic delimiters to define a subpopulation with
394 a single fluorescent protein (with or without an inert retrograde marker injected into separate sites
395 in the brain), our approach enables facile collateral mapping across the whole nervous system
396 with higher resolution that is growing in popularity (33,59,61). These results demonstrate that
397 despite the high complexity and repetitive nature of the *RR5* cassette, we could efficiently target
398 this allele, the allele remains stable through germline transmission, and it is responsive to Cre
399 and FLP recombinase expression. The restriction of expression to anatomically defined NA
400 neurons as a whole or as a projection subset further establishes the recombinase specificity of
401 our targeting schematic. This approach should also translate equally well to further anatomical,
402 functional, and molecular characterizations of NA and other subtypes defined by their projection
403 patterns with the use of the additional lines reported here.

404 Noradrenergic (NA) neurons are strongly implicated in control of respiratory homeostasis and
405 chemosensitivity (8,69–75), but many prior studies bear methodological caveats such as lack of

406 resolution due to overly broad lesions or injections (76), developmental and non-cell-autonomous
407 compensation after gene mutations, or restraint or anesthesia *in vivo* (77). Here we show in
408 conscious, unrestrained mice that inhibition of *TgDBH-Cre*-defined noradrenergic neurons led to
409 significantly reduced tidal volume and minute ventilation following hypercapnic exposure. On the
410 other hand, activation of *TgDBH-Cre*-defined noradrenergic neurons led to significantly increased
411 respiratory rate, tidal volume, and minute ventilation in the room air breathing condition. These
412 data represent modulation of the noradrenergic system that significantly deviates from previously
413 published studies interrogating this system and provides an alternative to those investigating
414 control of breathing that reduces the influence of possible side effects or unintended effects.

415 In conclusion, the methods presented here represent a significant improvement in feasibility and
416 affordability for labs to generate their own intersectional mouse models for investigating circuit
417 development. Our vector design and application allow for large cassettes to be targeted to the
418 *Rosa26* locus with high throughput, increased efficiency, germline transmission, and preserved
419 pluripotency. These protocols and techniques can be used to investigate most, if not all, neural
420 circuits in the context of development and/ or disease. Implementing these techniques also serve
421 as an alternative to cost-prohibitive commercially available vectors and mouse lines. Together,
422 we present a facile, cost-effective method for producing gene specific intersectional mouse lines
423 for neural circuit investigation.

CONCLUSIONS

During development, many distinct neuronal and glial subtypes arise and intercalate to create the complex neural circuits that govern our behavior and physiology. Key to understanding this organization and how it may be perturbed in neurological diseases is the ability to identify and access discrete cell subtypes in the developing and adult mouse nervous systems for multi-faceted studies. It is now clear that even within narrowly defined cell types once thought as homogeneous, significant diversity is found at multiple levels including genetic and molecular signatures, activity patterns, synaptic connectivity, and projection patterns. Given this complexity, it is often difficult to define and access specific cellular populations for study, particularly during embryogenesis, where *in utero* development makes access problematic.

The power of studying combinatorially defined neuronal populations increases significantly when multiple distinct neuronal features, such as birthdate, collateral projection targets, molecular profiles, or a functional requirement in a given physiological process or behavior can be examined in parallel to reveal deeper insights into the mechanisms involved in the establishment and maintenance of neural circuit organization. However, the ability to carry out such studies is restricted by the limited number of publicly available intersectional mouse lines as well as the inherent difficulty in developing new intersectional alleles.

We present a novel CRISPR/Cas9-mediated system for consistently targeting large cassettes to the *Rosa26* locus for high throughput and parallel generation of intersectional and conditional mouse lines. These studies demonstrate that CRISPR/Cas9 can be used to increase targeting efficiency at the *Rosa26* locus in mouse embryonic stem cells with shortened 1-1.2 kb homology arms while preserving pluripotency and the ability to transmit alleles via the germline. This technology allows for the opportunity to generate mouse lines that express a wide range of effector molecules in neural cell types, enabling the developmental, anatomical, molecular, and

448 functional characterization of neural circuit organization in behavior and physiology. To
449 democratize the generation of intersectional and conditional targeted ES cells and mouse lines,
450 we have generated a publicly available vector toolkit for single-step cloning into *Rosa26*-targeting
451 vectors for double and single-recombinase responsive cassettes (**Table 1).** We have also
452 generated several mouse lines available, without restriction, to the not-for-profit research
453 community enabling high specificity intersectional access of neuronal and other populations for
454 cross correlative mapping approaches using functional neuronal perturbation, molecular profiling,
455 and anatomical characterizations for multifaceted studies (**Table 2**). Overall, these resources and
456 the modular nature of the intersectional approach make rapid and low-cost production of large
457 numbers of intersectional alleles possible that can be efficiently distributed as ES cells or mouse
458 lines throughout the mouse research community. All vectors (Addgene; 97007-97012, 99142),
459 mouse lines (MMRRC; 043513-043519), and ES cells (BCM ES Cell Core Facility) have been
460 made publicly and unconditionally available to the academic research community.

461 **METHODS**

462 **Construction of targeting and Cas9 vectors**: The simplified *Rosa26* targeting vector was
463 derived using standard cloning procedures from a targeting vector used in previous studies (49)
464 consisting of a p15a origin of replication, kanamycin selection cassette, DTA negative selection
465 cassette, and *Rosa26* homology (1081 bp 5' homology arm and 4342 bp 3' homology arm). The
466 total vector size was 9084 bps. The DTA was removed and the 5' homology arm was shortened
467 to 1025 bp fragment (deleting the sgRNA target sequence) while the 3' homology arm was
468 shortened to 1231 bps, reducing the total vector length to 4694 bps and eliminating a number of
469 repetitive regions that often resulted in vector instability when constructing intersectional targeting
470 vectors.

471 For the Cas9 expressing vector, we selected an sgRNA target sequence that was close to the 5'
472 and 3' junction of the *Rosa26* gene locus (ACTGGAGTTGCAGATCACGA with PAM motif GGG).
473 The selected sgRNA was cloned into the BbsI sites of the px330 vector that expresses Cas9 (final
474 vector is called *px330_Rosa26_sgRNA*).

475 Knock-in cassettes were assembled in either 1) a previously used intersectional template plasmid
476 (*RR1-4, RR6-7*); 2) a newly constructed intersectional template plasmid with neomycin promoter
477 and pA elements removed (*RR5* and *RR8*); or 3) a constructed Dre-responsive template plasmid
478 (*RR9* and *RR10*). The intersectional plasmid consisted of a ubiquitous *CAG* promoter sequence;
479 an *FRT*-flanked stop cassette consisting of a PGK-neo sequence (for positive selection of
480 targeted ES cells) and three *SV40 pA* sequences; a *LoxP*-flanked stop cassette containing
481 mCherry and a PBS302 stop cassette; and a cloning site for insertion followed by a *WPRE* and
482 *BGHpA* sequence. The new intersectional template consisted of a ubiquitous *CAG* promoter
483 sequence; an *FRT* flanked stop cassette consisting of a neomycin sequence and *His3_SV40 pA*;
484 a *LoxP*-flanked subtractive cloning site stop cassette consisting of a *His3_SV40 pA*; and a cloning

485 site for insertion followed by *WPRE* and *BGHpA* sequences. The Dre-responsive template
486 consisted of a *Rox*-flanked stop cassette consisting of a neomycin sequence and PBS302 stop
487 cassette, and a cloning site followed by a *WPRE* and *BGHpA* sequence.

488 For assembly of complete targeting vectors, the cDNAs of interest were PCR amplified and cloned
489 into the corresponding vector. The intersectional or Dre-responsive cassettes were then cut out
490 with PacI or PacI/AscI and cloned into the shortened *Rosa26* targeting vector.

491 To facilitate single step cloning of complete targeting vectors, we generated a vector toolkit (**Table**
492 **1)** by constructing and moving empty *CAG* cassettes in the Rosa26 targeting vector. We
493 generated four template vectors with neomycin resistance: 1) a Cre/FLP responsive targeting
494 vector; 2) Cre only; 3) FLP only; and 4) Dre-responsive targeting vector. The intersectional
495 template vector consists of the *CAG* promoter, an *FRT*-flanked neomycin resistance gene and
496 stop cassette, a subtractive cloning site (EcoRV) and stop cassette flanked by *LoxP* sites, an
497 intersectional cloning site (PmeI), and *WPRE* and *BHGpA* elements. Each single template vector
498 consists of the *CAG* promoter, stop cassette(s) and neomycin resistance cassette flanked by
499 recombinase sites, cloning site (SwaI), and *WPRE* and *bgh polyA* elements. Additionally, for
500 possible direct oocyte injections we also generated a Cre/FLP responsive targeting vector that
501 does not contain a neomycin resistance gene, with a subtractive cloning site (EcoRV) and
502 intersectional cloning site (SwaI). All cloning sites are blunt restriction enzyme sites for cloning
503 facilitation.

504 Sequences of the template vectors and *px330* vector and plasmids are available through Addgene
505 (provisional ID #s 97007-97012, 99142).

506 **Generation of knock-in mice:** Embryonic stem (ES) cells (AB2.2) were electroporated with 15-
507 20 µg of varying ratios of the *px330_Rosa26_sgRNA* vector to the targeting vector. Neomycin
508 selected clones were screened for homologous recombination using PCR genotyping. Targeted

509 clones were identified using PCR genotyping for 5' and 3' targeting from outside the homology
510 arm and were considered to be successful targeting events if positive for both 5' and 3'
511 genotyping. We used pairs 5'CGCCTAAAGAAGAGGCTGTG (Rosa26-F) and
512 5'GGGCGTACTTGGCATATGAT (CAG-R), producing a 1450 bp band; and
513 5'AATCAACCTCTGGATTACAAAATTT (WPRE-F) and 5'TGGCTCCTCTGTCCACAGTT
514 (Rosa26-R), producing a 2472 bp band.

515 Select targeted clones were microinjected into C57B1/J6 blastocysts and chimeric males were
516 bred to wildtype C57B1/J6 females to achieve germline transmission.

517 **Pronuclear injection**: We constructed a targeting vector by cloning a calcium indicator, Twitch-
518 2B (52), into the Cre responsive *Rosa26* targeting vector. The Baylor College of Medicine
519 Embryonic Stem (ES) Cell Core generated the *Rosa26*-specific sgRNA and Cas9 protein for
520 injection. Pronuclear injections were performed by the Baylor College of Medicine Genetically
521 Engineered Mouse (GEM) Core using the following parameters: 30 ng/µl Cas9 protein, 20 ng/µl
522 sgRNA, and 2 ng/µl dsDNA plasmid. Potential founders were screened for targeting as described
523 above.

524 **Breeding, genetic background, and maintenance of mice**: We maintained colonies of select
525 mouse strains by backcrossing to C57BL/6J mice. For routine genotyping, we carried out PCR
526 amplification of DNA from ear punch preparations using the boiling alkaline lysis procedure.
527 *Rosa26* specific primers for the mice were 5'-GCACTTGCTCTCCCAAAGTC, 5'-
528 GGGCGTACTTGGCATATGAT, and 5'-CTTTAAGCCTGCCCAGAAGA, and yield a 495 bp band
529 (targeted) and 330 bp band (wt). For histology experiments, *RR5* mice were bred to
530 *DBH*^{p2aFLPo}(51)*; B6N.FVB-Tmem163*$^{Tg(ACTB\text{-}cre)2Mrt}$*/CjDswJ (Bactin-Cre)* and *DBH*^{p2aFLPo} mice. For
531 plethysmography experiments, *B6.FVB(Cg)-Tg(Dbh-Cre)KH212Gsat/Mmucd (DBH-Cre)* mice
532 were mated with homozygous Cre-only responsive *RR1P* and *RR2P* mice (after crossing

533 intersectional alleles to *B6;SJL-Tg(ACTFLPe)9205Dym/J* [JAX 003800] mice to recombine out
534 the FLP-responsive stop cassette followed by homozygosity) to derive animals in which all mice
535 carried the Cre-responsive hM4D or hM3D allele. Sibling animals that did not inherit the *Cre* allele
536 were used as control animals to the *Cre* positive offspring. For electrophysiology experiments,
537 *DBH-Cre; RR2P* mice were mated to *RC::ePe* mice expressing a floxed eGFP. Cre-specific
538 primers were 5'-ATCGCCATCTTCCAGCAGGCGCACCATTGCCC and 5'-
539 GCATTTCTGGGGATTGCTTA and yielded a 550 bp band if positive. FLPo-specific primers were
540 5'CACGCCCAGGTACTTGTTCT and 5'CCACAGCAAGAAGATGCTGA and yielded a 226 bp
541 band if positive.

542 Established mouse lines reside at the Mutant Mouse Regional Resource Center (MMRRC) and
543 will be unconditionally available to the academic research community (MMRRC 043513-043519).
544 Targeted ES cells have been archived and are available upon request under the condition that
545 any new mouse lines are deposited in a public repository.

546 All animal experiments were performed with the approval of IACUC.

547 **Off-target analysis**: Off-target sequences were identified using the Optimized CRISPR Design
548 tool (crispr.mit.edu). The top 5 sequences for each sgRNA were amplified from selected targeted
549 ES cells and sequenced to determine if any mutations or changes occurred in off-target sites.

550 **Viral injection**: To test the functionality of the *RR5* mouse strain, adult *RR5* mice were injected
551 with equal titers of AAV9-hSyn-FLPo and AAV1-hSyn-Cre viruses (obtained from M. Xue at BCM,
552 250 nl at 1.12×10^{12} GC/mL) into the dentate gyrus (coordinates from bregma AP=-2.70, DV=-
553 2.12, ML=1.84) and with equal titers of AAV-EF1a-Cre-WPRE and AAV-EF1a-FLPo-WPRE (UNC
554 Vector Core, 250 nl at 5.06×10^{11} GC/mL) into the amygdala (coordinates from bregma AP=-1.06,
555 DV=-4.61, ML=-2.86) and allowed to incubate for 7-14 days. For expression in the olfactory bulb,
556 adult *RR5* mice were injected with AAV-CAG-Cre (obtained from Neuroconnectivity Core at Jan

557 and Dan Duncan Neurological Research Institute, AAV2/9 690 μL at $5.37x10^{13}$ pp/mL) and AAV-
558 Ef1a-Flp (obtained from Neuroconnectivity Core at Jan and Dan Duncan Neurological Research
559 Institute, AAV2/9 690 μL at $7.16x10^{11}$ pp/mL) into the core of the olfactory bulb (coordinates from
560 bregma AP=4.5mm, DV=-2.25mm, ML=±0.8mm) and allowed to incubate for 14 days. For the
561 CAV2-Cre virus experiments, *RR5; DBH^{p2aFLP}* mice were injected with CAV2-Cre virus (IGMM
562 Viral Core, 500 nL at $6.0x10^{12}$ pp/mL) into the amygdala (coordinates -2.86, -1.06, -4.61) and
563 allowed to incubate for 17 days. For the Retro-AAV-Ef1a-FLPo virus experiments, *RR5;*
564 *Vglut2_Cre* mice were injected with Retro-FLPo virus (obtained from Neuroconnectivity Core at
565 Jan and Dan Duncan Neurological Research Institute, 690 μL at $1.49x10^{12}$ pp/mL) into the lateral
566 hypothalamic area (coordinates from bregma AP=-1.22mm, DV=-5.12mm, ML=±0.97mm) and
567 allowed to incubate for 21 days.

568 **Histology**: For *RR5* expression, animals were sacrificed and transcardially perfused with 0.1M
569 phosphate-buffered saline (PBS) then with 4% paraformaldehyde (PFA) in PBS. Brains were
570 dissected out and drop fixed for two hours in 4% PFA before a PBS rinse and equilibration in 20%
571 sucrose in PBS. Brains were sectioned into 30-40 μm coronal sections and mounted on slides.
572 Images were collected on a Zeiss confocal LSM780 microscope or Leica TCS SPE confocal
573 microscope.

574 **Electrophysiology**

575 ***Slice preparation***

576 Slice preparation from the mouse LC follows an N-Methyl-D-glucamine (NMDG) slicing protocol
577 (78,79). Briefly, animals were deeply anesthetized using 3% isoflurane. After decapitation, the
578 brain was removed and placed into cold (0−4 °C) oxygenated NMDG solution containing 93 mM
579 NMDG, 93 mM HCl, 2.5 mM KCl, 1.2 mM NaH_2PO_4, 30 mM $NaHCO_3$, 20 mM HEPES, 25 mM
580 glucose, 5 mM sodium ascorbate, 2 mM Thiourea, 3 mM sodium pyruvate, 10mM $MgSO_4$ and 0.5

581 mM $CaCl_2$, pH 7.35 (all from SIGMA-ALDRICH). Horizontal slices were prepared using a
582 vibratome (200 µm thick) using zirconia blades. The brain slices were kept at 37.0 ± 0.5 °C in
583 oxygenated NMDG solution for 10 minutes. They were then transferred to an artificial
584 cerebrospinal fluid (ACSF) containing 125 mM NaCl, 2.5 mM KCl, 1.25 mM NaH_2PO_4, 25 mM
585 $NaHCO_3$, 1 mM $MgCl_2$, 25 mM glucose, and 2 mM $CaCl_2$ (pH 7.4) for at least 1 hour prior to the
586 beginning of recordings. During the recording sessions, the slices were submerged in a custom
587 chamber and were stabilized with a fine nylon net attached to a custom-designed platinum ring.
588 This recording chamber was continuously perfused with oxygenated physiological solution
589 throughout the recording session.

590 ***Recordings***

591 Whole-cell recordings were performed as described previously (79–81). Briefly, patch pipettes (2-
592 8 MΩ) were filled with an internal solution containing 120 mM potassium gluconate, 10 mM
593 HEPES, 4 mM KCl, 4 mM MgATP, 0.3 mM Na_3GTP, 10 mM sodium phosphocreatine and 0.5%
594 biocytin (pH 7.25). Whole-cell recordings from up to 8 LC neurons were performed using two
595 Quadro EPC 10 amplifiers (HEKA Electronic, Germany). PatchMaster (HEKA) and custom-written
596 Matlab-based programs (Mathworks) were used to operate the recording system and perform
597 online and offline data analysis. In current-clamp recordings, neurons were first current clamped
598 at ~-40pA to prevent spontaneous firing. Prior to investigating the effect of drugs, we calculated
599 spike thresholds and recorded firing patterns in response to sustained depolarizing currents by
600 injecting increasing current steps (+10pA). Continuous recordings were obtained from LC neurons
601 current clamped at -40 to 0 pA during drug wash-on experiments. We also calculated other
602 intrinsic electrophysiological parameters, such as the input resistance, membrane time constant,
603 spike amplitude, after-hyperpolarization (AHP) etc. (79–81).

604 **Plethysmography**

605 Plethysmography on conscious, unrestrained mice was carried out as described on 6-12 week
606 old adult animals (49,82). Mice were subjected to a five-day habituation protocol with each day
607 consisting of several minutes of handling, temperature taken by rectal probe, intraperitoneal saline
608 injection, and 30 minutes in the plethysmography chamber. Mice were then tested within one
609 week of the last day of conditioning.

610 On the day of testing, mice were taken from their home cage, weighed, and rectal temperature
611 was taken. Animals were then placed into an airtight, temperature controlled (~32°C)
612 plethysmography chamber and allowed to acclimate for at least 20 minutes in room air (21%
613 O_2/79% N_2) conditions. After acclimation and measurement under room air, the chamber gas was
614 switched to a hypercapnic mixture of 5% CO_2/21% O_2/74% N_2 for 20 minutes. Chamber gas was
615 then switched back to room air for 20 minutes. The mice were briefly removed for rectal
616 temperature measurement and intra-peritoneal injection of clozapine-N-oxide (CNO, National
617 Institute of Mental Health Chemical Synthesis and Drug Supply Program) dissolved in saline (0.1
618 mg/mL) for an effective concentration 1 mg/kg. The animal was returned to the chamber for
619 another 20 minutes of room air, 20 minutes of hypercapnia, and 20 minutes of room air. The
620 animal was then removed from the chamber and rectal temperature was taken immediately
621 afterwards and again 30 minutes after the termination of the experiment. The animal was placed
622 in its own cage during these 30 minutes at the ambient room temperature (~23°C).

623 ***Plethysmography data collection and analysis***

624 Plethysmography pressure changes were measured using a Validyne DP45 differential pressure
625 transducer and CD15 carrier demodulator in comparison to a reference chamber and recorded
626 with LabChartPro in real time. Waveforms were analyzed offline using LabChart Pro and custom
627 written MATLAB code to determine respiratory rate (V_f), tidal volume (V_T) (49), minute ventilation
628 ($\dot{V}_E$), and pattern analysis. Respiratory waveforms were collected offline during periods when the

629 animal was at rest and readings were free from movement artifacts. A minimum of 1-minute
630 cumulative data compiled from traces at least 10 seconds long from the last 10 minutes of a given
631 experimental condition were analyzed. O_2 consumption was determined by comparing the gas
632 composition between calibration in an empty chamber and live breathing using an AEI oxygen
633 sensor and analyzer. Chamber temperature was constantly monitored and recorded using a
634 ThermoWorks MicroThermo 2 and probe and was recorded with LabChartPro in real time.

635 ***Plethysmography statistics***

636 Results (V_f, V_T, $\dot{V}_E$, $\dot{V}_{O2}$, $\dot{V}_E/\dot{V}_{O2}$) for room air and hypercapnic data were compared between all
637 cohorts using a linear mixed-effects regression model with animal type (experimental or control)
638 and CNO administration (pre- or post-injection) as fixed effects and animal ID as a random effect.
639 Temperature data was compared using a linear mixed-effects regression model with animal type
640 (experimental or control) as a fixed effect. The p-values reported correspond to statistical
641 significance of the conditional interaction between animal type and CNO administration. A p-value
642 of <0.05 was used to indicate statistical significance and standard error of the mean is shown on
643 all charts.

644 **Imaging of Twitch 2 in mouse preovulatory follicles**

645 Preovulatory follicles were isolated and imaged as previously described (83). Briefly, antral
646 follicles were dissected from 23- to 26-d-old *RR8; Bact_Cre mice*. Follicles were cultured for 24–
647 30 h on organotypic membranes (Millipore) in the presence of follicle-stimulating hormone. The
648 follicle was held in a perfusion slide consisting of a plastic slide (ibidi) and a glass coverslip and
649 assembled using silicon grease. The slide was constructed such that medium containing ovine
650 LH (National Hormone and Peptide Program; 10 µg/mL) could be perfused through a 200-µm-
651 deep channel holding the follicle. Temperature was maintained at 30–34 °C, by use of a warm air

652 blower (Nevtek). Preovulatory Follicles were imaged using a Zeiss Pascal confocal microscope
653 with a 40X/1.2 NA objective. Images were collected every 10 sec. Measurements were corrected
654 for autofluorescence and for spectral bleed-through of CFP into the YFP channel. Ratios were
655 calculated by dividing the mean CFP intensity in each region of interest by the mean YFP intensity.
656 Data analysis was done using ImageJ and Excel software. Data is representative of 4 follicles.

657 # Declarations

658 **Ethics approval and consent to participate**

659 All experiments reported herein were conducted with explicit approval of and oversight by both
660 Baylor College of Medicine Institutional Animal Care and Use Committee (IACUC) and University
661 of Connecticut IACUC and abide by all state and national regulations regarding animal research
662 for each work site.

663 **Consent for publication**

664 Not applicable.

665 **Availability of data and materials**

666 All datasets, animals, and materials generated and/ or used in this study are publicly available
667 (Addgene and Mutant Mouse Resource and Research Centers Supported by NIH (MMRRC)) or
668 available from the corresponding author on reasonable request.

669 **Competing interests**

670 The authors declare no competing interests.

671 **Funding**

672 R01: H1130249 (RR)

673 R21: OD025327 (RR)

674 R37: HD014939 (JRE and Laurinda A. Jaffe)

675 **Authors' contributions**

676 SJL completed experiments, analyzed data, and prepared the manuscript.

677 AM completed experiments, analyzed data, and prepared the manuscript.

678 JJS completed experiments, analyzed data, and prepared the manuscript.

679 PJH completed experiments, analyzed data, and prepared the manuscript.

680 PGF completed experiments, analyzed data and prepared the manuscript.

681 JP completed experiments, analyzed data, and prepared the manuscript.

682 VKM assisted in the completion of experiments.

683 JRE completed experiments, analyzed data, and prepared the manuscript.

684 PJZ completed experiments, analyzed data and prepared the manuscript

685 XJ completed experiments, analyzed data, and prepared the manuscript.

686 BRA completed experiments, analyzed data, and prepared the manuscript.

687 AST completed experiments, analyzed data and prepared the manuscript

688 M C-M assisted with experimental design and prepared the manuscript

689 RR conceptualized the study, performed experiments, analyzed data, and prepared the
690 manuscript.

691 All authors read and approved the final manuscript.

692 **Acknowledgements**

693 We thank M. Xue for providing the Cre and FLPo AAV viruses used in the dentate gyrus injection
694 and Ronda Kram for technical assistance with cloning, mouse husbandry, and maintenance. We
695 thank J. Dougherty, E. Schuman, J. Wess, B. Roth, and S. Sternson for providing plasmid
696 templates for the EGFP-L10A, MetRS, G_s-D, hM4D and hM3D, and PSAM cDNA, respectively.
697 We thank Laurinda A. Jaffe for collaborating with us and author JRE with the Twitch studies. The
698 Baylor College of Medicine Embryonic Stem (ES) Cell Core performed the ES cell
699 electroporations and were exceptionally helpful in our experiments and the Baylor College of
700 Medicine Genetically Engineered Mouse (GEM) Core performed the blastocyst injections.
701 Imaging was carried out at the Baylor College of Medicine Optical Imaging and Vital Microscopy
702 Core.

703 **Table 1. Publicly available modular targeting vectors for rapid generation of recombinase-**

704 **responsive ES cells and mouse lines.**

705 **Table 2. *Rosa26* knock-in alleles generated with or without CRISPR/Cas9 methods.** Shown
706 are targeted *Rosa26* alleles, function, length of cassette, current status, and expected MGI name
707 (to be determined) in grey rows.

708 **Table 3. Targeting efficiencies for a multiplexed five cassette ES cell electroporation for**

709 **the *Rosa26* locus.**

710 **Figure 1. Generation of intersectional *Rosa26* mouse lines**. **A)** Targeting schematic showing
711 the modular targeting vector containing a 1kb 5' homology arm, *CAG* promoter, *FRT*-flanked
712 neomycin and stop cassette, *LoxP*-flanked (optional) subtractive gene of interest (GOI-S) and
713 stop cassette, intersectional gene of interest (GOI-I), *WPRE*, *bgh poly A* element, and 1.2kb 3'
714 homology arm. The full intersectional cassette was knocked into the *Rosa26* locus, with a 22 bp
715 deletion of the CRISPR sgRNA. **B)** PCR genotyping of neomycin selected ES cell clones.
716 Targeting knock-in was determined using PCR primers that spanned from outside the *Rosa26*
717 homology arms to either the *CAG* promoter (5' end) or *WPRE* (3' end). Amplification of a band
718 indicates targeting. Shown are results from a targeting event with over 60% targeting efficiency
719 (*RR7*). **C)** Four conditions with different Cas9:targeting vector ratios were used in our initial study:
720 a 0:1 with no Cas9, 0.5:1, 1:1, and 10:1 **D)** Targeting efficiency results from the different ratios.
721 The 10:1 Cas9:targeting vector ratio showed a 5-10 fold increase over an electroporation with no
722 Cas9. Shown in red are results from previous electroporations using the traditional Rosa26
723 targeting vector with more commonly used longer homology arms.

724 **Figure 2. Analysis of *Rosa26* sgRNA off-target sites**. No mutations were seen in the top 5
725 potential off-target sites. **A)** List of top 10 potential off-target sites as determined by the Optimized
726 CRISPR tool, base pair mismatches, and location in the genome. **B-F)** Sequence chromatograms
727 of each off-target site, showing the correct sequence for each of the 3 selected clones that were
728 injected into blastocysts as compared to the wildtype sequence.

729 **Figure 3. Germline Cre/FLP expression in *RR5* adult mice to fluorescently label three**
730 **cellular compartments in targeted cells. A-H)** *RR5* mice bred to *DBH*^{p2aFLP}*; Bactin-Cre* mice
731 express Cre ubiquitously and FLP in all noradrenergic (NA) neurons, thus marking only NA
732 neurons, including the locus coeruleus (**A-D**) and A5 nucleus (**E-H**). **I-P)** *RR5* mice bred to
733 *Vgat_Cre; Vglut2-FLPo* mice with dual recombinase expression imaged in the entopeduncular
734 nucleus (**I-L**) and lateral habenula (**M-P**). In targeted cells that express both Cre and FLP, cell
735 nuclei are labeled with TagBFP, cell soma and processes are labeled with sfGFP, and pre-
736 synaptic contacts are labeled with tdTomato.

737 **Figure 4. Viral-mediated expression of Cre or FLP recombinase in *RR5* adult mice to**

738 **simultaneously, fluorescently label three cellular components.** *RR5* mice injected with

739 equal titers of AAV-Cre and AAV-FLP viruses into the dentate gyrus (**A-H**), basolateral

740 amygdala (**I-P**), and olfactory bulb (**Q-T**).

741 **Figure 5. Retrograde-viral Cre and germline FLP mediated expression of dual**
742 **recombinases for tricistronic FP expression on *RR5* background. A)** *RR5; DBH*^{p2aFLPo} mice
743 were injected with CAV2-Cre virus into the basolateral amygdala. All *DBH* noradrenergic neurons
744 express FLP, but only those noradrenergic neurons projecting to the injected amygdala will also
745 express Cre. Marked double Cre/FLP positive cells will express H2B-TagBFP highlighting the
746 nucleus in blue, sfGFP filling the cell including the axon, and synaptophysin-tdTomato labeling
747 presynaptic contacts. BLA: Basolateral amygdala. DG: Dentate gyrus. DR: Dorsal raphé. LC:
748 Locus coeruleus. OB: Olfactory bulb. RtTg: Reticulotegmental pontine nucleus. *DBH* positive
749 neurons that project to the amygdala arise primarily from the ipsilateral locus coeruleus (**B-E**) with
750 some sparse labeling in the contralateral locus coeruleus (**F-I**). Red puncta overlapping with green
751 but lacking blue marked nuclei (indicative of projections from the marked population) can be seen
752 in a variety of mid- and forebrain areas, including the injected amygdala (**J-M**), the raphé nucleus
753 (**N-Q**), reticulotegmental pontine nuclei (**R-U**), dentate gyrus (**V-Y**), and olfactory bulb (**Z-CC**).

754 **Figure 6. Retrograde-viral FLP and germline Cre mediated expression of dual**
755 **recombinases for tricistronic FP expression on *RR5* background. A)** *RR5; Vglut2^{Cre}* mice
756 were injected with retro-AAV-Ef1a-FLPo virus into the lateral hypothalamus. All *Vglut2* neurons
757 express Cre, but only those Vglut2 neurons projecting to the injected LHA will also express FLP.
758 Marked double Cre/FLP positive cells will express H2B-TagBFP highlighting the nucleus in blue,
759 sfGFP filling the cell including the axon, and synaptophysin-tdTomato labeling presynaptic
760 contacts. LHA: Lateral hypothalamic area. Vglut2 positive neurons that project to the LHA arise
761 from the cingulate gyrus (**B-E**), piriform cortex (**F-I**), and medial habenula (**J-M**).

762 **Figure 7. Electrophysiological characterization of CNO-DREADD mediated responses in**
763 **lines *RR1(P)* *RR2(P)* and *RC::FPDi* *(P)* in noradrenergic *DBH-Cre* Locus Coeruleus**
764 **neurons.** **(A)** Representative wash-on responses for each *RR1(P) (n=19*
765 *neurons), RR2(P) (n=10 neurons),* and *RC::FPDi*(P) *(n=10 neurons)* in response to DREADD
766 agonists. **(B)** Individual membrane potential plots of pre-CNO vs post-CNO values. **(C)** Summary
767 plots of absolute voltage change for each DREADD line tested following CNO treatment. *p<0.05;
768 **p<0.01; ***p<0.001.

769 **Figure 8. CNO-hM4D mediated perturbation of noradrenergic *DBH-Cre* neurons results in**
770 **a reduced hypercapnic response. A)** Representative breathing traces from a *DBH-Cre; RR1P*
771 animal before and after CNO administration under hypercapnic conditions
772 (5%CO_2/21%O_2/74%N_2). **B-F)** Quantification of respiratory and metabolic parameters under room
773 air and hypercapnic conditions in *DBH-Cre; RR1P* animals and sibling controls. Measured values
774 include respiratory rate (**B)**, tidal volume (**C)**, minute ventilation **(D)**, oxygen consumption **(E)**, and
775 minute ventilation normalized to oxygen consumption **(G)**. No difference was seen under room air
776 conditions but *DBH-Cre; RR1P* animals showed a deficit in volume, minute ventilation, and minute
777 ventilation normalized to oxygen consumption under hypercapnic conditions. **G)** No difference in
778 temperature was seen between *DBH-Cre; RR1P* animals and sibling controls. *$p<0.05$; **$p<0.01$;
779 ***$p<0.001$.

780 **Figure 9. CNO-hM3D mediated perturbation of noradrenergic *DBH-Cre* neurons results in**
781 **enhanced room air ventilation and a reduced hypercapnic response. A)** Representative
782 breathing traces from a *DBH-Cre; RR2P* animal before and after CNO administration under
783 room air conditions (21%O_2/79%N_2). **B)** Representative breathing traces from a *DBH-Cre;*
784 *RR2P* animal before and after CNO administration under hypercapnic conditions
785 (5%CO_2/21%O_2/74%N_2). **C-G)** Quantification of respiratory and metabolic parameters under
786 room air and hypercapnic conditions in *DBH-Cre; RR2P* animals and sibling controls. Measured
787 values include respiratory rate (**C)**, tidal volume (**D)**, minute ventilation **(E)**, oxygen consumption
788 **(F)**, and minute ventilation normalized to oxygen consumption **(G)**. After CNO administration,
789 *DBH-Cre; RR2P* animals showed increase rate, volume, minute ventilation, and oxygen
790 consumption under room air conditions. Under hypercapnic conditions, *DBH-Cre; RR2P* animals
791 showed increased oxygen consumption resulting in a reduced minute ventilation to oxygen
792 consumption value. **I)** *DBH-Cre; RR2P* animals showed a significant deficit in temperature 30
793 minutes after the end of the assay. *$p<0.05$; **$p<0.01$; ***$p<0.001$.

794 **Figure 10. Expression and function of Twitch-2B in the granulosa cells of mouse ovarian**
795 **follicles.** (**A**) A follicle from a mouse expressing Twitch-2B (homozygote). A follicle consists of
796 multiple layers of granulosa cells surrounding an oocyte in the center. Twitch-2B is uniformly
797 expressed in the granulosa cells but is not detectable in the oocyte. A layer of theca cells,
798 adhering to the outside of the follicle, expresses Twitch-2B at a higher level. Scale bar = 50 μm.
799 (**B**) ~6-fold increase in YFP/CFP ratio in the outer granulosa cells after application of 10 μM
800 ionomycin in the presence of 10 mM $CaCl_2$. Representative of 4 follicles.

REFERENCES

1. Armbruster BN, Li X, Pausch MH, Herlitze S, Roth BL. Evolving the lock to fit the key to create a family of G protein-coupled receptors potently activated by an inert ligand. Proc Natl Acad Sci USA. 2007 Mar 20;104(12):5163–8.
2. Sauer B. Manipulation of transgenes by site-specific recombination: Use of cre recombinase. Guide to techniques in mouse development. Elsevier; 1993. p. 890–900.
3. Chuong AS, Miri ML, Busskamp V, Matthews GAC, Acker LC, Sørensen AT, et al. Noninvasive optical inhibition with a red-shifted microbial rhodopsin. Nat Neurosci. 2014 Aug;17(8):1123–9.
4. Rowitch DH, S-Jacques B, Lee SM, Flax JD, Snyder EY, McMahon AP. Sonic hedgehog regulates proliferation and inhibits differentiation of CNS precursor cells. J Neurosci. 1999 Oct 15;19(20):8954–65.
5. Urlinger S, Baron U, Thellmann M, Hasan MT, Bujard H, Hillen W. Exploring the sequence space for tetracycline-dependent transcriptional activators: novel mutations yield expanded range and sensitivity. Proc Natl Acad Sci USA. 2000 Jul 5;97(14):7963–8.
6. Sander JD, Joung JK. CRISPR-Cas systems for editing, regulating and targeting genomes. Nat Biotechnol. 2014 Apr;32(4):347–55.
7. Platt RJ, Chen S, Zhou Y, Yim MJ, Swiech L, Kempton HR, et al. CRISPR-Cas9 knockin mice for genome editing and cancer modeling. Cell. 2014 Oct 9;159(2):440–55.
8. Dubreuil V, Ramanantsoa N, Trochet D, Vaubourg V, Amiel J, Gallego J, et al. A human mutation in Phox2b causes lack of CO2 chemosensitivity, fatal central apnea, and specific loss of parafacial neurons. Proc Natl Acad Sci USA. 2008 Jan 22;105(3):1067–72.
9. Zucker SN, Bancroft TA, Place DE, Des Soye B, Bagati A, Berezney R. A dominant negative Cx43 mutant differentially affects tumorigenic and invasive properties in human metastatic melanoma cells. J Cell Physiol. 2013 Apr;228(4):853–9.
10. LeMaster AM, Krimm RF, Davis BM, Noel T, Forbes ME, Johnson JE, et al. Overexpression of brain-derived neurotrophic factor enhances sensory innervation and selectively increases neuron number. J Neurosci. 1999 Jul 15;19(14):5919–31.
11. Collins AL, Levenson JM, Vilaythong AP, Richman R, Armstrong DL, Noebels JL, et al. Mild overexpression of MeCP2 causes a progressive neurological disorder in mice. Hum Mol Genet. 2004 Nov 1;13(21):2679–89.
12. Ellis T, Smyth I, Riley E, Bowles J, Adolphe C, Rothnagel JA, et al. Overexpression of Sonic Hedgehog suppresses embryonic hair follicle morphogenesis. Dev Biol. 2003 Nov 15;263(2):203–15.
13. Ngo JT, Champion JA, Mahdavi A, Tanrikulu IC, Beatty KE, Connor RE, et al. Cell-selective metabolic labeling of proteins. Nat Chem Biol. 2009 Oct;5(10):715–7.
14. Doyle JP, Dougherty JD, Heiman M, Schmidt EF, Stevens TR, Ma G, et al. Application of a translational profiling approach for the comparative analysis of CNS cell types. Cell. 2008 Nov 14;135(4):749–62.
15. Marvin JS, Borghuis BG, Tian L, Cichon J, Harnett MT, Akerboom J, et al. An optimized fluorescent probe for visualizing glutamate neurotransmission. Nat Methods. 2013 Feb;10(2):162–70.
16. Akemann W, Mutoh H, Perron A, Park YK, Iwamoto Y, Knöpfel T. Imaging neural circuit dynamics with a voltage-sensitive fluorescent protein. J Neurophysiol. 2012 Oct;108(8):2323–37.
17. Lin C-W, Sim S, Ainsworth A, Okada M, Kelsch W, Lois C. Genetically increased cell-intrinsic excitability enhances neuronal integration into adult brain circuits. Neuron. 2010 Jan 14;65(1):32–9.
18. Johns DC, Marx R, Mains RE, O'Rourke B, Marbán E. Inducible genetic suppression of neuronal excitability. J Neurosci. 1999 Mar 1;19(5):1691–7.
19. Ibañez-Tallon I, Wen H, Miwa JM, Xing J, Tekinay AB, Ono F, et al. Tethering naturally occurring peptide toxins for cell-autonomous modulation of ion channels and receptors in vivo. Neuron. 2004 Aug 5;43(3):305–11.

852 20. Duan B, Cheng L, Bourane S, Britz O, Padilla C, Garcia-Campmany L, et al. Identification of
853 spinal circuits transmitting and gating mechanical pain. Cell. 2014 Dec 4;159(6):1417–32.
854 21. Kim JC, Cook MN, Carey MR, Shen C, Regehr WG, Dymecki SM. Linking genetically defined
855 neurons to behavior through a broadly applicable silencing allele. Neuron. 2009 Aug 13;63(3):305–
856 15.
857 22. Conklin BR, Hsiao EC, Claeysen S, Dumuis A, Srinivasan S, Forsayeth JR, et al. Engineering
858 GPCR signaling pathways with RASSLs. Nat Methods. 2008 Aug;5(8):673–8.
859 23. Beier KT, Samson MES, Matsuda T, Cepko CL. Conditional expression of the TVA receptor
860 allows clonal analysis of descendents from Cre-expressing progenitor cells. Dev Biol. 2011 May
861 15;353(2):309–20.
862 24. Magnus CJ, Lee PH, Atasoy D, Su HH, Looger LL, Sternson SM. Chemical and genetic
863 engineering of selective ion channel-ligand interactions. Science. 2011 Sep 2;333(6047):1292–6.
864 25. Vardy E, Robinson JE, Li C, Olsen RHJ, DiBerto JF, Giguere PM, et al. A new DREADD
865 facilitates the multiplexed chemogenetic interrogation of behavior. Neuron. 2015 May
866 20;86(4):936–46.
867 26. Zhao R, Grunke SD, Keralapurath MM, Yetman MJ, Lam A, Lee T-C, et al. Impaired Recall of
868 Positional Memory following Chemogenetic Disruption of Place Field Stability. Cell Rep. 2016 Jul
869 19;16(3):793–804.
870 27. Beier KT, Saunders A, Oldenburg IA, Miyamichi K, Akhtar N, Luo L, et al. Anterograde or
871 retrograde transsynaptic labeling of CNS neurons with vesicular stomatitis virus vectors. Proc Natl
872 Acad Sci USA. 2011 Sep 13;108(37):15414–9.
873 28. Wickersham IR, Finke S, Conzelmann K-K, Callaway EM. Retrograde neuronal tracing with a
874 deletion-mutant rabies virus. Nat Methods. 2007 Jan;4(1):47–9.
875 29. Zeisel A, Muñoz-Manchado AB, Codeluppi S, Lönnerberg P, La Manno G, Juréus A, et al. Brain
876 structure. Cell types in the mouse cortex and hippocampus revealed by single-cell RNA-seq.
877 Science. 2015 Mar 6;347(6226):1138–42.
878 30. Fuzik J, Zeisel A, Máté Z, Calvigioni D, Yanagawa Y, Szabó G, et al. Integration of
879 electrophysiological recordings with single-cell RNA-seq data identifies neuronal subtypes. Nat
880 Biotechnol. 2016 Feb;34(2):175–83.
881 31. Cadwell CR, Palasantza A, Jiang X, Berens P, Deng Q, Yilmaz M, et al. Electrophysiological,
882 transcriptomic and morphologic profiling of single neurons using Patch-seq. Nat Biotechnol. 2016
883 Feb;34(2):199–203.
884 32. Dymecki SM, Ray RS, Kim JC. Mapping Cell Fate and Function Using Recombinase-Based
885 Intersectional Strategies. Guide to Techniques in Mouse Development, Part B: Mouse Molecular
886 Genetics, 2nd Edition. Elsevier; 2010. p. 183–213.
887 33. Robertson SD, Plummer NW, de Marchena J, Jensen P. Developmental origins of central
888 norepinephrine neuron diversity. Nat Neurosci. 2013 Aug;16(8):1016–23.
889 34. Brust RD, Corcoran AE, Richerson GB, Nattie E, Dymecki SM. Functional and developmental
890 identification of a molecular subtype of brain serotonergic neuron specialized to regulate breathing
891 dynamics. Cell Rep. 2014 Dec 24;9(6):2152–65.
892 35. Niederkofler V, Asher TE, Okaty BW, Rood BD, Narayan A, Hwa LS, et al. Identification of
893 Serotonergic Neuronal Modules that Affect Aggressive Behavior. Cell Rep. 2016 Nov
894 15;17(8):1934–49.
895 36. Ruffault P-L, D'Autréaux F, Hayes JA, Nomaksteinsky M, Autran S, Fujiyama T, et al. The
896 retrotrapezoid nucleus neurons expressing Atoh1 and Phox2b are essential for the respiratory
897 response to CO_2. Elife. 2015 Apr 13;4.
898 37. He M, Tucciarone J, Lee S, Nigro MJ, Kim Y, Levine JM, et al. Strategies and tools for
899 combinatorial targeting of gabaergic neurons in mouse cerebral cortex. Neuron. 2016 Sep
900 21;91(6):1228–43.
901 38. Madisen L, Garner AR, Shimaoka D, Chuong AS, Klapoetke NC, Li L, et al. Transgenic mice for
902 intersectional targeting of neural sensors and effectors with high specificity and performance.

903 Neuron. 2015 Mar 4;85(5):942–58.
904 39. Chen Y-W, Das M, Oyarzabal EA, Cheng Q, Plummer NW, Smith KG, et al. Genetic identification
905 of a population of noradrenergic neurons implicated in attenuation of stress-related responses. Mol
906 Psychiatry. 2019;24(5):710–25.
907 40. Tervo DGR, Hwang B-Y, Viswanathan S, Gaj T, Lavzin M, Ritola KD, et al. A designer AAV
908 variant permits efficient retrograde access to projection neurons. Neuron. 2016 Oct 19;92(2):372–
909 82.
910 41. Zingg B, Chou X-L, Zhang Z-G, Mesik L, Liang F, Tao HW, et al. AAV-Mediated Anterograde
911 Transsynaptic Tagging: Mapping Corticocollicular Input-Defined Neural Pathways for Defense
912 Behaviors. Neuron. 2017 Jan 4;93(1):33–47.
913 42. Kawano F, Okazaki R, Yazawa M, Sato M. A photoactivatable Cre-loxP recombination system for
914 optogenetic genome engineering. Nat Chem Biol. 2016 Dec;12(12):1059–64.
915 43. Tang JCY, Rudolph S, Dhande OS, Abraira VE, Choi S, Lapan SW, et al. Cell type-specific
916 manipulation with GFP-dependent Cre recombinase. Nat Neurosci. 2015 Sep;18(9):1334–41.
917 44. DeNardo LA, Liu CD, Allen WE, Adams EL, Friedmann D, Fu L, et al. Temporal evolution of
918 cortical ensembles promoting remote memory retrieval. Nat Neurosci. 2019 Jan 28;22(3):460–9.
919 45. Quadros RM, Miura H, Harms DW, Akatsuka H, Sato T, Aida T, et al. Easi-CRISPR: a robust
920 method for one-step generation of mice carrying conditional and insertion alleles using long
921 ssDNA donors and CRISPR ribonucleoproteins. Genome Biol. 2017 May 17;18(1):92.
922 46. Allen WE, Luo L. Intersectional illumination of neural circuit function. Neuron. 2015 Mar
923 4;85(5):889–92.
924 47. Zambrowicz BP, Imamoto A, Fiering S, Herzenberg LA, Kerr WG, Soriano P. Disruption of
925 overlapping transcripts in the ROSA beta geo 26 gene trap strain leads to widespread expression of
926 beta-galactosidase in mouse embryos and hematopoietic cells. Proc Natl Acad Sci USA. 1997 Apr
927 15;94(8):3789–94.
928 48. Soriano P. Generalized lacZ expression with the ROSA26 Cre reporter strain. Nat Genet. 1999
929 Jan;21(1):70–1.
930 49. Ray RS, Corcoran AE, Brust RD, Kim JC, Richerson GB, Nattie E, et al. Impaired respiratory and
931 body temperature control upon acute serotonergic neuron inhibition. Science. 2011 Jul
932 29;333(6042):637–42.
933 50. Cong L, Ran FA, Cox D, Lin S, Barretto R, Habib N, et al. Multiplex genome engineering using
934 CRISPR/Cas systems. Science. 2013 Feb 15;339(6121):819–23.
935 51. Sun JJ, Ray R. Generation of Two Noradrenergic-Specific Dopamine-Beta-Hydroxylase-FLPo
936 Knock-In Mice Using CRISPR/Cas9-Mediated Targeting in Embryonic Stem Cells. PLoS One.
937 2016 Jul 21;11(7):e0159474.
938 52. Thestrup T, Litzlbauer J, Bartholomäus I, Mues M, Russo L, Dana H, et al. Optimized ratiometric
939 calcium sensors for functional in vivo imaging of neurons and T lymphocytes. Nat Methods. 2014
940 Feb;11(2):175–82.
941 53. Alexander GM, Rogan SC, Abbas AI, Armbruster BN, Pei Y, Allen JA, et al. Remote control of
942 neuronal activity in transgenic mice expressing evolved G protein-coupled receptors. Neuron. 2009
943 Jul 16;63(1):27–39.
944 54. Guettier J-M, Gautam D, Scarselli M, Ruiz de Azua I, Li JH, Rosemond E, et al. A chemical-
945 genetic approach to study G protein regulation of beta cell function in vivo. Proc Natl Acad Sci
946 USA. 2009 Nov 10;106(45):19197–202.
947 55. Heiman M, Kulicke R, Fenster RJ, Greengard P, Heintz N. Cell type-specific mRNA purification
948 by translating ribosome affinity purification (TRAP). Nat Protoc. 2014 May 8;9(6):1282–91.
949 56. Li L, Tasic B, Micheva KD, Ivanov VM, Spletter ML, Smith SJ, et al. Visualizing the distribution
950 of synapses from individual neurons in the mouse brain. PLoS One. 2010 Jul 9;5(7):e11503.
951 57. Hnasko TS, Perez FA, Scouras AD, Stoll EA, Gale SD, Luquet S, et al. Cre recombinase-mediated
952 restoration of nigrostriatal dopamine in dopamine-deficient mice reverses hypophagia and
953 bradykinesia. Proc Natl Acad Sci USA. 2006 Jun 6;103(23):8858–63.

954 58. Soudais C, Laplace-Builhe C, Kissa K, Kremer EJ. Preferential transduction of neurons by canine
955 adenovirus vectors and their efficient retrograde transport in vivo. FASEB J. 2001
956 Oct;15(12):2283–5.
957 59. Plummer NW, Chandler DJ, Powell JM, Scappini EL, Waterhouse BD, Jensen P. An Intersectional
958 Viral-Genetic Method for Fluorescent Tracing of Axon Collaterals Reveals Details of
959 Noradrenergic Locus Coeruleus Structure. Eneuro. 2020 May 15;7(3).
960 60. Rodríguez CI, Buchholz F, Galloway J, Sequerra R, Kasper J, Ayala R, et al. High-efficiency
961 deleter mice show that FLPe is an alternative to Cre-loxP. Nat Genet. 2000 Jun;25(2):139–40.
962 61. Jensen P, Farago AF, Awatramani RB, Scott MM, Deneris ES, Dymecki SM. Redefining the
963 serotonergic system by genetic lineage. Nat Neurosci. 2008 Apr;11(4):417–9.
964 62. Egbert JR, Fahey PG, Reimer J, Owen CM, Evsikov AV, Nikolaev VO, et al. Follicle-stimulating
965 hormone and luteinizing hormone increase Ca2+ in the granulosa cells of mouse ovarian follicles†.
966 Biol Reprod. 2019 May 14;
967 63. Quadros RM, Miura H, Harms DW, Akatsuka H, Sato T, Aida T, et al. Easi-CRISPR: a robust
968 method for one-step generation of mice carrying conditional and insertion alleles using long
969 ssDNA donors and CRISPR ribonucleoproteins. Genome Biol. 2017 May 17;18(1):92.
970 64. Wang B, Li K, Wang A, Reiser M, Saunders T, Lockey RF, et al. Highly efficient CRISPR/HDR-
971 mediated knock-in for mouse embryonic stem cells and zygotes. BioTechniques. 2015 Oct
972 1;59(4):201–2, 204, 206.
973 65. Chu VT, Weber T, Graf R, Sommermann T, Petsch K, Sack U, et al. Efficient generation of Rosa26
974 knock-in mice using CRISPR/Cas9 in C57BL/6 zygotes. BMC Biotechnol. 2016 Jan 16;16:4.
975 66. Yoshimi K, Kunihiro Y, Kaneko T, Nagahora H, Voigt B, Mashimo T. ssODN-mediated knock-in
976 with CRISPR-Cas for large genomic regions in zygotes. Nat Commun. 2016 Jan 20;7:10431.
977 67. Bang SJ, Jensen P, Dymecki SM, Commons KG. Projections and interconnections of genetically
978 defined serotonin neurons in mice. Eur J Neurosci. 2012 Jan;35(1):85–96.
979 68. Bochkov YA, Palmenberg AC. Translational efficiency of EMCV IRES in bicistronic vectors is
980 dependent upon IRES sequence and gene location. BioTechniques. 2006 Sep;41(3):283–4, 286,
981 288 passim.
982 69. Viemari J-C, Roux J-C, Tryba AK, Saywell V, Burnet H, Peña F, et al. Mecp2 deficiency disrupts
983 norepinephrine and respiratory systems in mice. J Neurosci. 2005 Dec 14;25(50):11521–30.
984 70. Viemari J-C, Ramirez J-M. Norepinephrine differentially modulates different types of respiratory
985 pacemaker and nonpacemaker neurons. J Neurophysiol. 2006 Apr;95(4):2070–82.
986 71. Li A, Emond L, Nattie E. Brainstem catecholaminergic neurons modulate both respiratory and
987 cardiovascular function. Adv Exp Med Biol. 2008;605:371–6.
988 72. Biancardi V, Bícego KC, Almeida MC, Gargaglioni LH. Locus coeruleus noradrenergic neurons
989 and CO2 drive to breathing. Pflugers Arch. 2008 Mar;455(6):1119–28.
990 73. Viemari J-C. Noradrenergic modulation of the respiratory neural network. Respir Physiol
991 Neurobiol. 2008 Dec 10;164(1–2):123–30.
992 74. Gargaglioni LH, Hartzler LK, Putnam RW. The locus coeruleus and central chemosensitivity.
993 Respir Physiol Neurobiol. 2010 Oct 31;173(3):264–73.
994 75. Kuo F-S, Falquetto B, Chen D, Oliveira LM, Takakura AC, Mulkey DK. In vitro characterization
995 of noradrenergic modulation of chemosensitive neurons in the retrotrapezoid nucleus. J
996 Neurophysiol. 2016 Sep 1;116(3):1024–35.
997 76. Engelbrecht AH, Russell V, Carstens ME, De Villiers AS, Searson A, Jaffer A, et al. Evidence that
998 noradrenergic neurons in the A1 and A2 nuclei are lesioned by low doses of 6-OHDA injected into
999 the locus coeruleus. J Neurosci Methods. 1994 Apr;52(1):57–60.
1000 77. Massey CA, Iceman KE, Johansen SL, Wu Y, Harris MB, Richerson GB. Isoflurane abolishes
1001 spontaneous firing of serotonin neurons and masks their pH/CO_2 chemosensitivity. J Neurophysiol.
1002 2015 Apr 1;113(7):2879–88.
1003 78. Ting JT, Daigle TL, Chen Q, Feng G. Acute brain slice methods for adult and aging animals:
1004 application of targeted patch clamp analysis and optogenetics. Patch.

1005 79. Jiang X, Shen S, Cadwell CR, Berens P, Sinz F, Ecker AS, et al. Principles of connectivity among
1006 morphologically defined cell types in adult neocortex. Science. 2015 Nov 27;350(6264):aac9462.
1007 80. Scala F, Kobak D, Shan S, Bernaerts Y, Laturnus S, Cadwell CR, et al. Layer 4 of mouse neocortex
1008 differs in cell types and circuit organization between sensory areas. Nat Commun. 2019 Sep
1009 13;10(1):4174.
1010 81. Scala F, Kobak D, Bernabucci M, Bernaerts Y, Cadwell CR, Castro JR, et al. Phenotypic variation
1011 of transcriptomic cell types in mouse motor cortex. Nature. 2020 Nov 12;
1012 82. Martinez VK, Saldana-Morales F, Sun JJ, Zhu PJ, Costa-Mattioli M, Ray RS. Off-Target Effects of
1013 Clozapine-N-Oxide on the Chemosensory Reflex Are Masked by High Stress Levels. Front
1014 Physiol. 2019 May 22;10:521.
1015 83. Shuhaibar LC, Egbert JR, Norris RP, Lampe PD, Nikolaev VO, Thunemann M, et al. Intercellular
1016 signaling via cyclic GMP diffusion through gap junctions restarts meiosis in mouse ovarian
1017 follicles. Proc Natl Acad Sci USA. 2015 Apr 28;112(17):5527–32.
1018

Figure 1

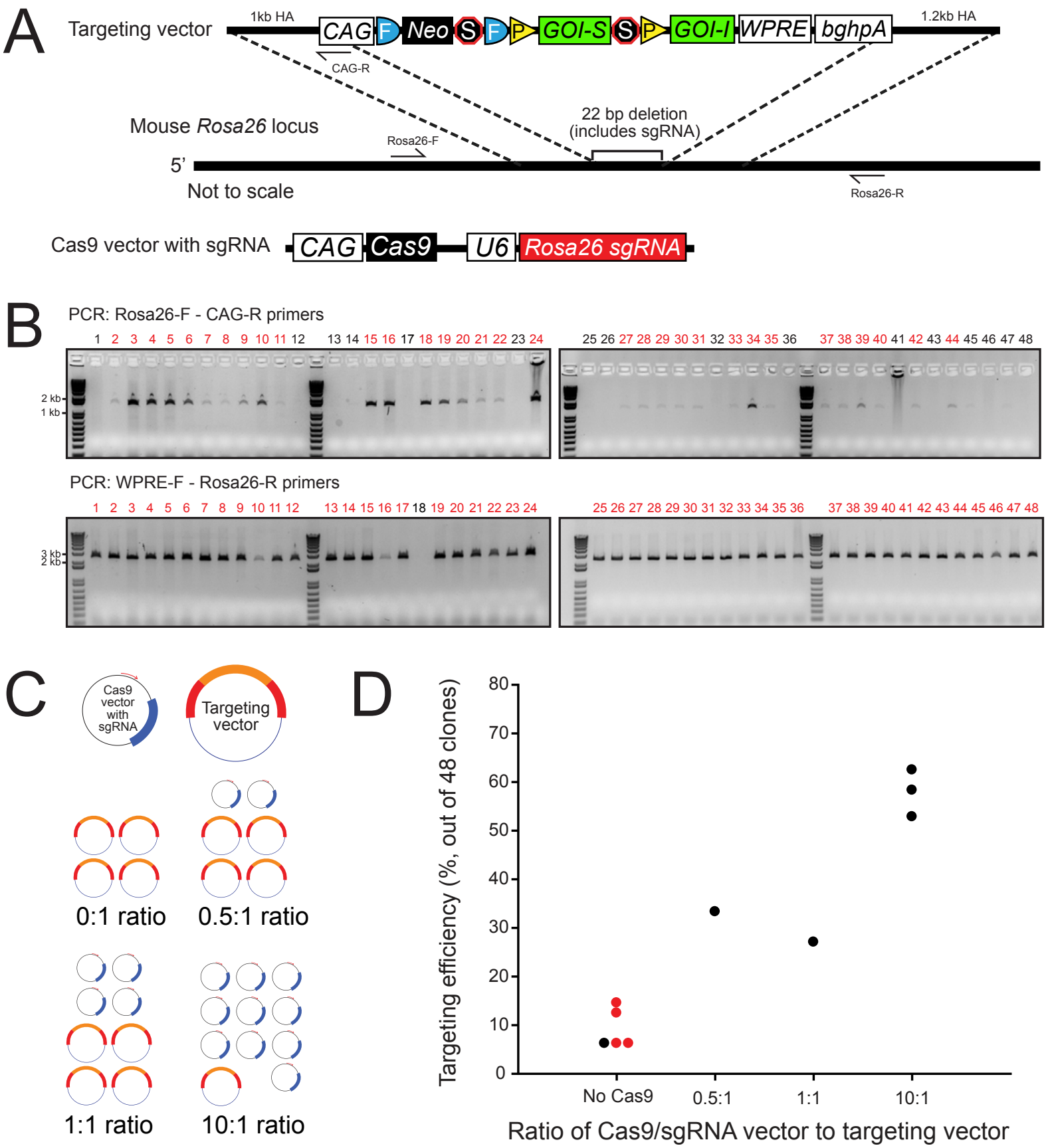
A
Targeting vector
1kb HA
CAG
F
Neo
S
F
P
GOI-S
S
P
GOI-I
WPRE
bghpA
1.2kb HA
CAG-R
Mouse Rosa26 locus
22 bp deletion
(includes sgRNA)
Rosa26-F
5'
Not to scale
Rosa26-R
Cas9 vector with sgRNA
CAG
Cas9
U6
Rosa26 sgRNA
B
PCR: Rosa26-F - CAG-R primers
2 kb
1 kb
PCR: WPRE-F - Rosa26-R primers
3 kb
2 kb
C
Cas9 vector with sgRNA
Targeting vector
0:1 ratio
0.5:1 ratio
1:1 ratio
10:1 ratio
D
Targeting efficiency (%, out of 48 clones)
No Cas9
0.5:1
1:1
10:1
Ratio of Cas9/sgRNA vector to targeting vector

Figure 2

A

	Sequence		Score	Mut	Locus
	ACTGGAGTTGCAGATCACGA	GGG			
Off1:	.T.T.....A.	CA.	1.1	3MM	chr15:-9941110
Off2:	C...TG...T.....	T..	0.8	4MM	chr14:-25087434
Off3:	C.....C.TG.....	TA.	0.7	4MM	chr9:+122854629
Off4:	.T..A....TT.....	.A.	0.7	4MM	chr6:-97126315
Off5:	TA..C.....T	AA.	0.7	4MM	chr16:-4397663
Off6:	.T.....G.....A.	AA.	0.7	3MM	chr10:+35384261
Off7:	.A..A..A.....T.	A..	0.5	4MM	chr11:-82755370
Off8:	.....AT.C.....	AA.	0.5	3MM	chr6:-124885038
Off9:	..G.T....T.....T.	T..	0.5	4MM	chr6:-41845311
Off10:	.....C..C....A.....	CA.	0.5	3MM	chr12:+103941450
Off11:	C.....AC.....C...	...	0.4	4MM	chr13:+43290788
Off12:	.G.....AA.....C...	T..	0.4	4MM	chr8:+95318409
Off13:	....CT.....A..	.A.	0.4	3MM	chr1:+11497683
Off14:	.A..T...G.....A.	TA.	0.3	4MM	chr12:+13635268
Off15:	.A.A...G.....G..	...	0.3	4MM	chr6:+41114906

B

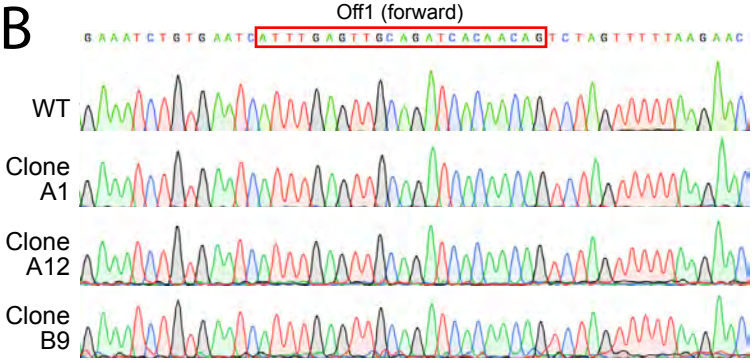

C

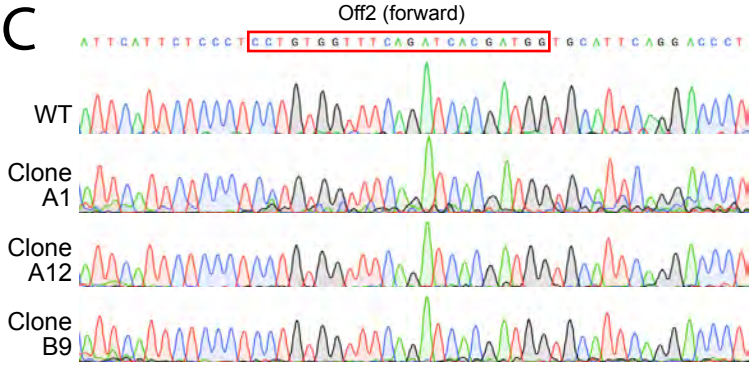

D

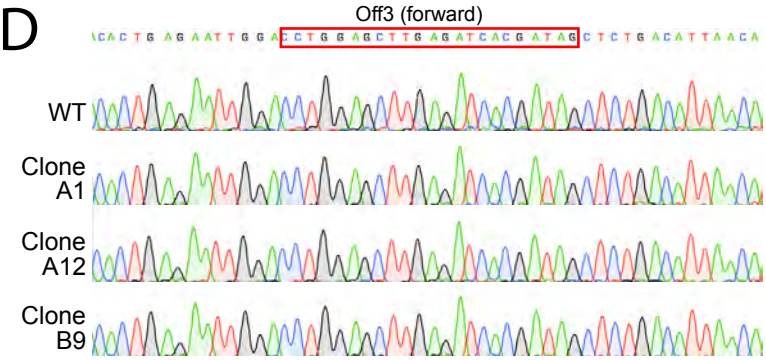

E

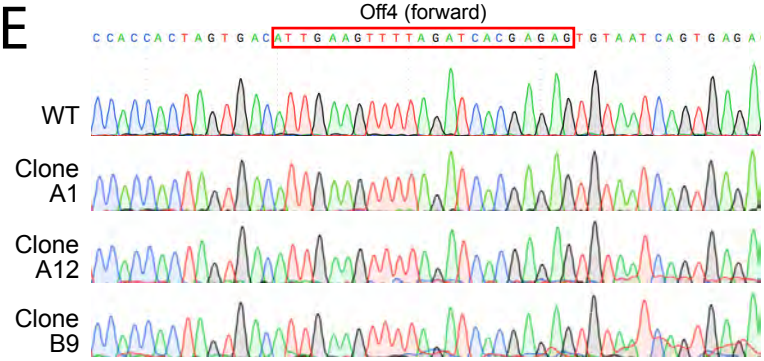

F

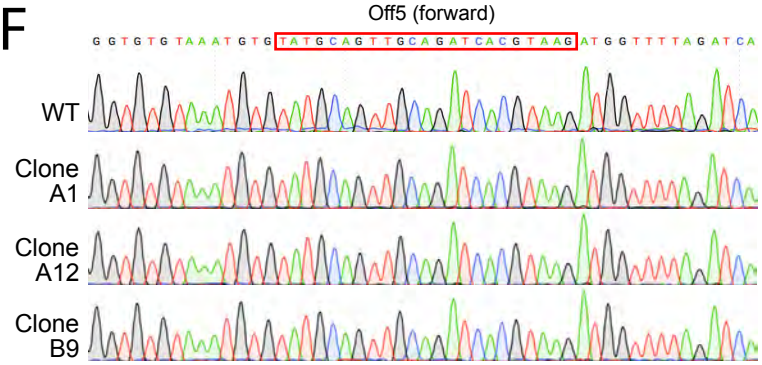

Figure 3

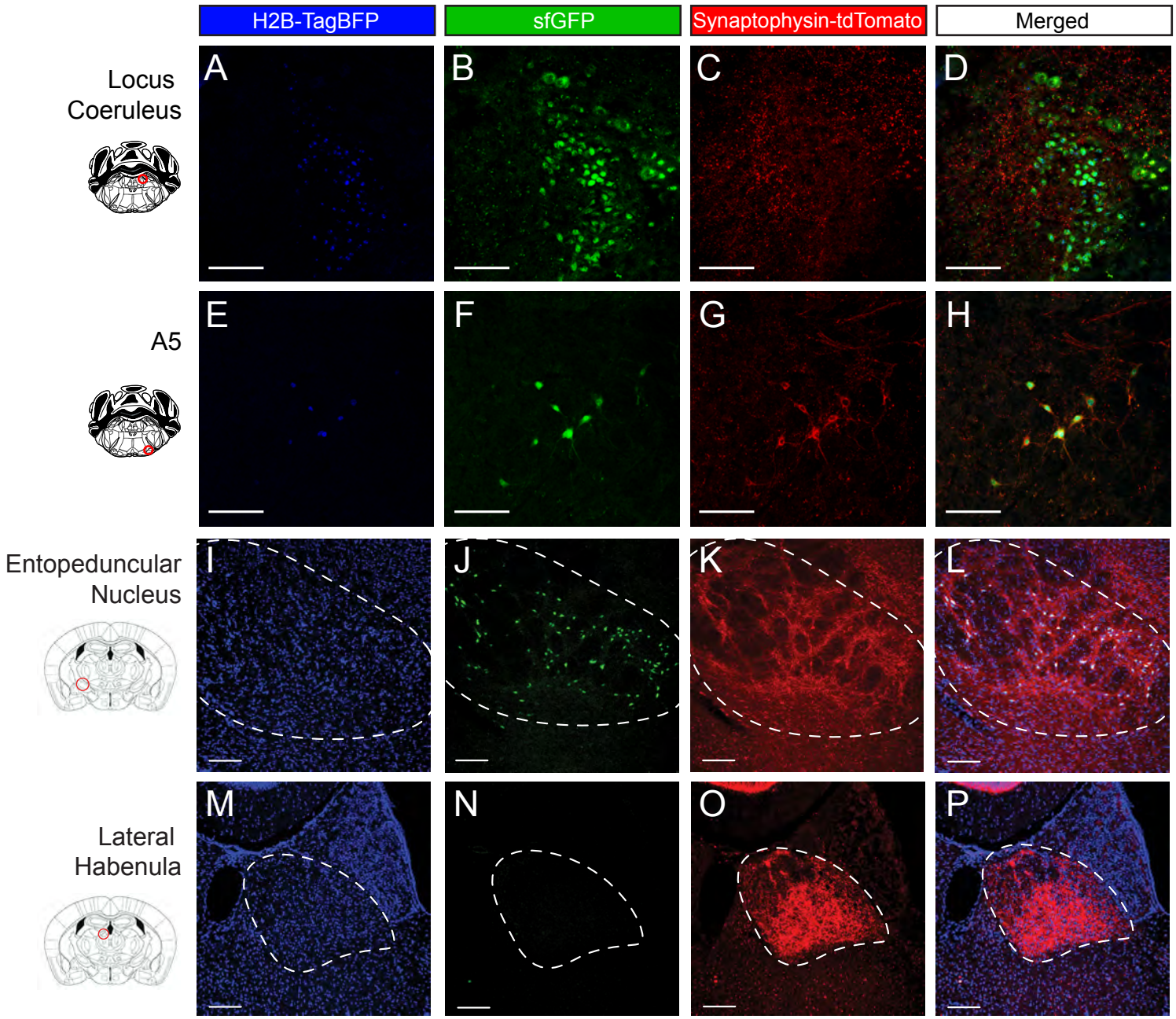
H2B-TagBFP
sfGFP
Synaptophysin-tdTomato
Merged
Locus Coeruleus
A5
Entopeduncular Nucleus
Lateral Habenula
A
B
C
D
E
F
G
H
I
J
K
L
M
N
O
P
Scale bar 50 μm

Figure 4

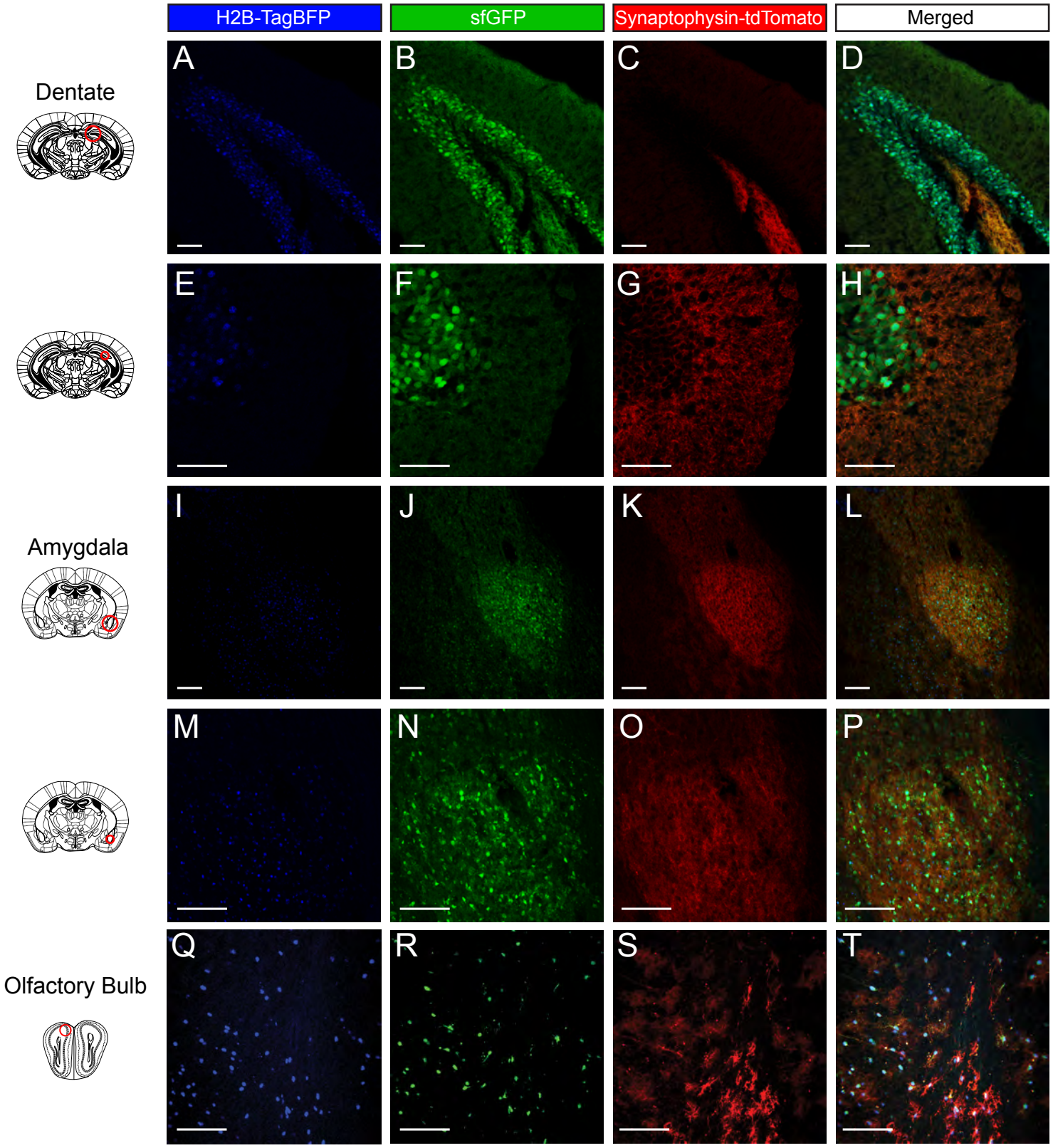
H2B-TagBFP
sfGFP
Synaptophysin-tdTomato
Merged
Dentate
Amygdala
Olfactory Bulb
A
B
C
D
E
F
G
H
I
J
K
L
M
N
O
P
Q
R
S
T
Scale bar 50 μm

Figure 5

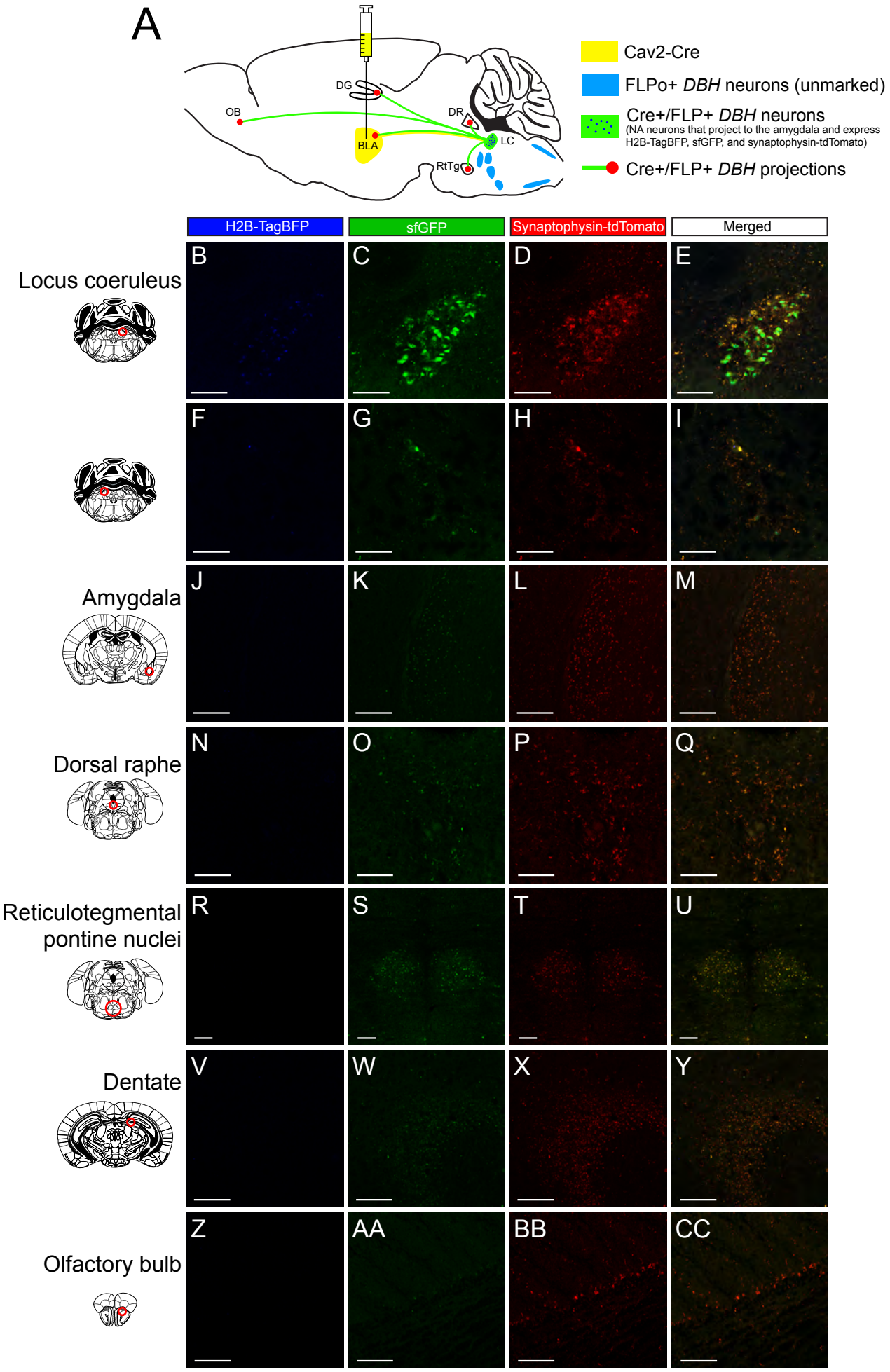
A
DG
OB
DR
BLA
LC
RtTg
Cav2-Cre
FLPo+ DBH neurons (unmarked)
Cre+/FLP+ DBH neurons
(NA neurons that project to the amygdala and express H2B-TagBFP, sfGFP, and synaptophysin-tdTomato)
Cre+/FLP+ DBH projections
H2B-TagBFP
sfGFP
Synaptophysin-tdTomato
Merged
Locus coeruleus
B
C
D
E
F
G
H
I
Amygdala
J
K
L
M
Dorsal raphe
N
O
P
Q
Reticulotegmental pontine nuclei
R
S
T
U
Dentate
V
W
X
Y
Olfactory bulb
Z
AA
BB
CC
Scale bar 50 μm

Figure 6

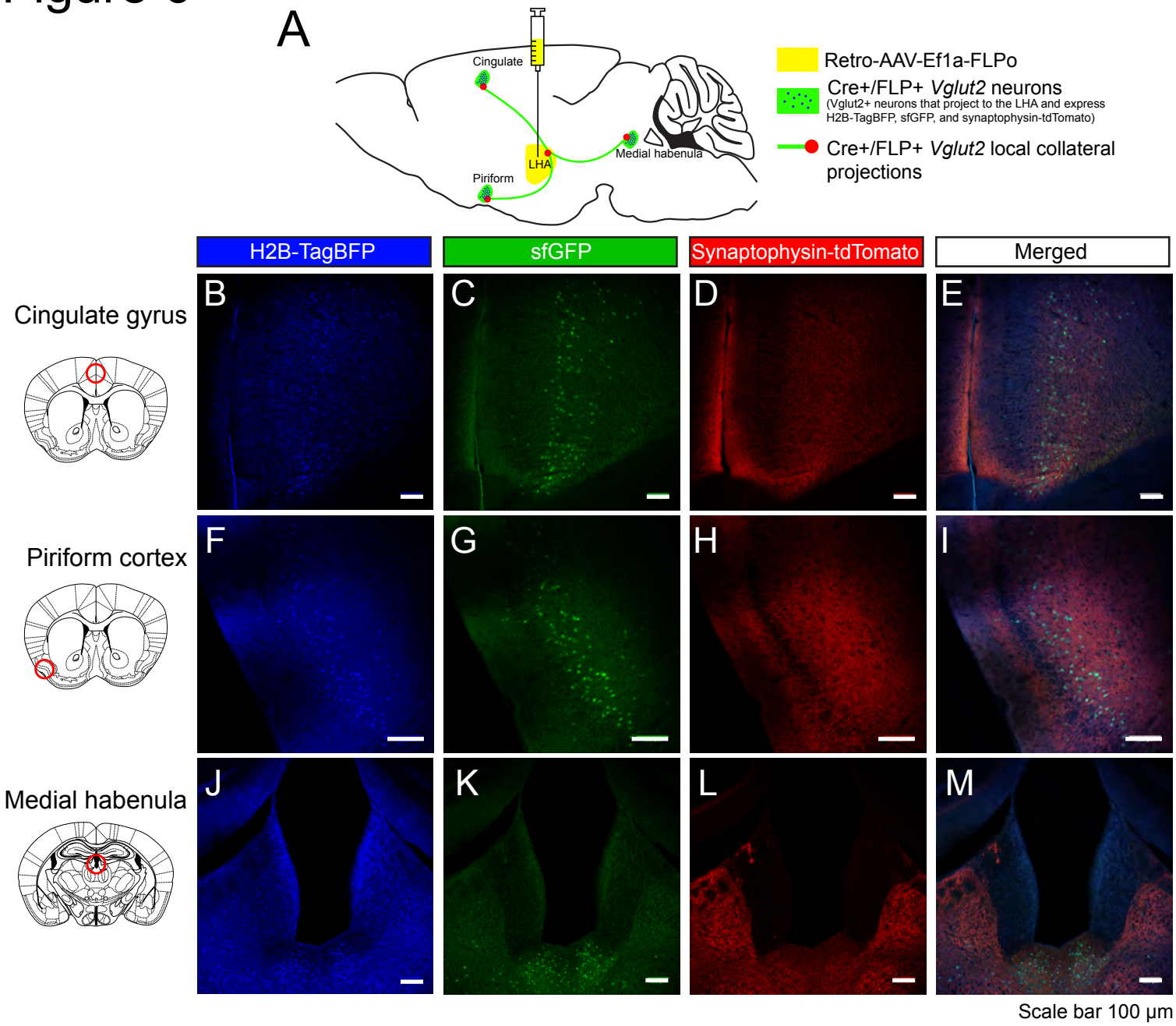

Scale bar 100 μm

Figure 7

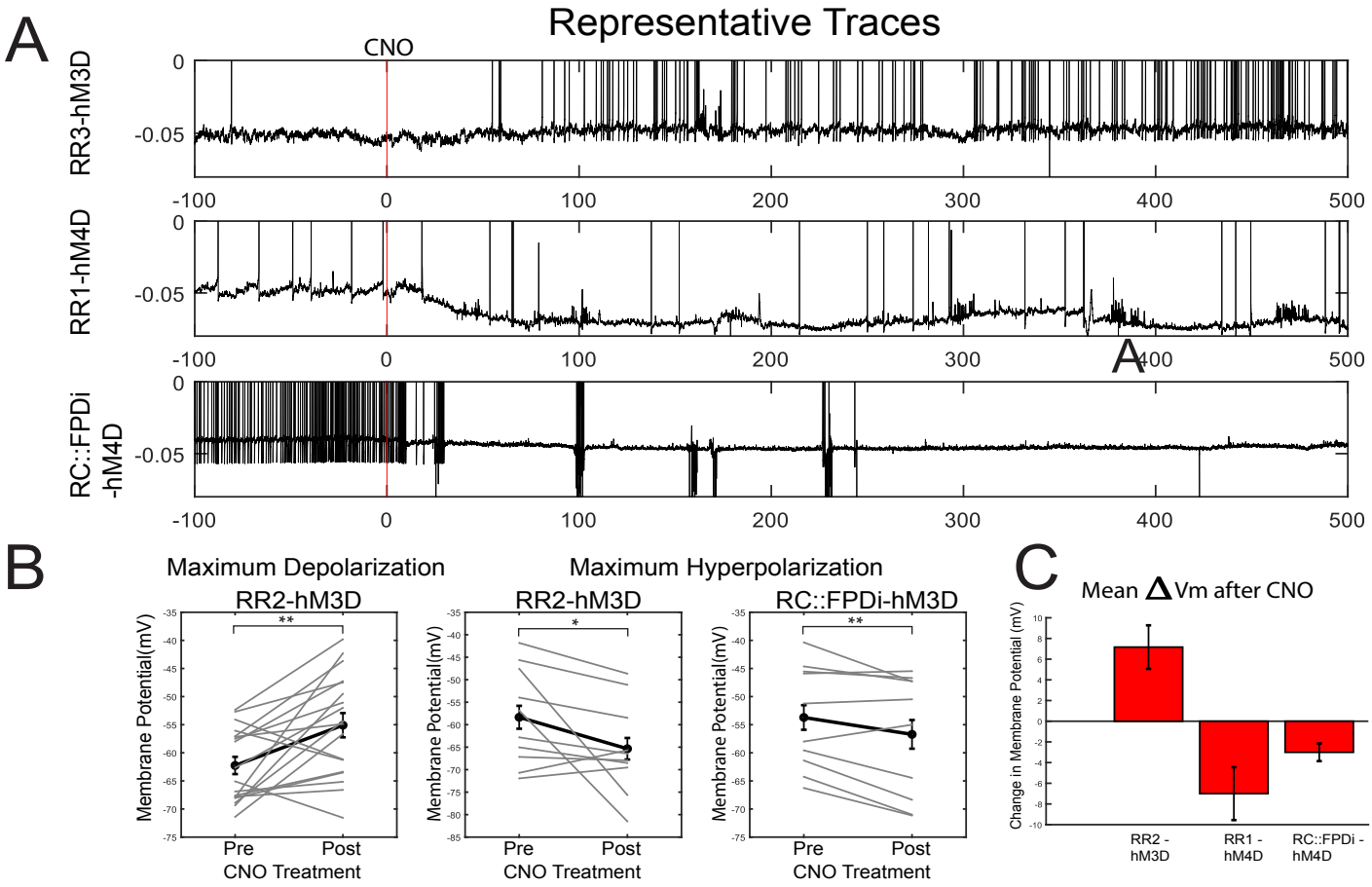
A
Representative Traces
CNO
RR3-hM3D
RR1-hM4D
RC::FPDi -hM4D
0
-0.05
-100
0
100
200
300
400
500
B
Maximum Depolarization
RR2-hM3D
Maximum Hyperpolarization
RR2-hM3D
RC::FPDi-hM3D
Membrane Potential(mV)
Pre
Post
CNO Treatment
**
*
C
Mean ΔVm after CNO
Change in Membrane Potential (mV)
RR2 - hM3D
RR1 - hM4D
RC::FPDi - hM4D

Figure 8

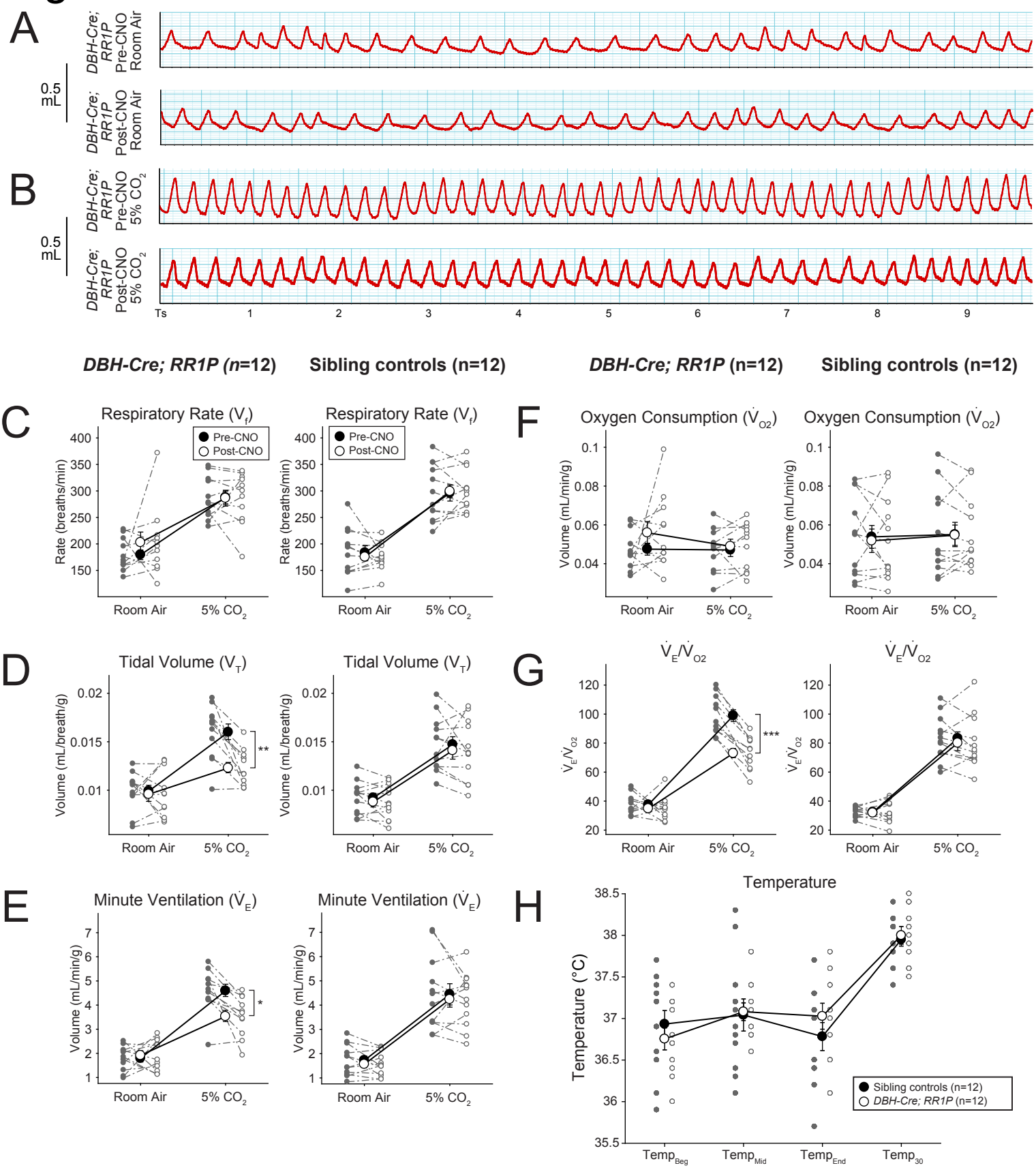
A
DBH-Cre; RR1P Pre-CNO Room Air
DBH-Cre; RR1P Post-CNO Room Air
0.5 mL
B
DBH-Cre; RR1P Pre-CNO 5% CO2
DBH-Cre; RR1P Post-CNO 5% CO2
0.5 mL
Ts 1 2 3 4 5 6 7 8 9
DBH-Cre; RR1P (n=12)
Sibling controls (n=12)
DBH-Cre; RR1P (n=12)
Sibling controls (n=12)
C
Respiratory Rate (Vf)
Pre-CNO
Post-CNO
Rate (breaths/min)
Room Air
5% CO2
D
Tidal Volume (VT)
Volume (mL/breath/g)
**
E
Minute Ventilation (VE)
Volume (mL/min/g)
*
F
Oxygen Consumption (VO2)
Volume (mL/min/g)
G
VE/VO2
***
H
Temperature
Temperature (°C)
Sibling controls (n=12)
DBH-Cre; RR1P (n=12)
TempBeg
TempMid
TempEnd
Temp30

Figure 9

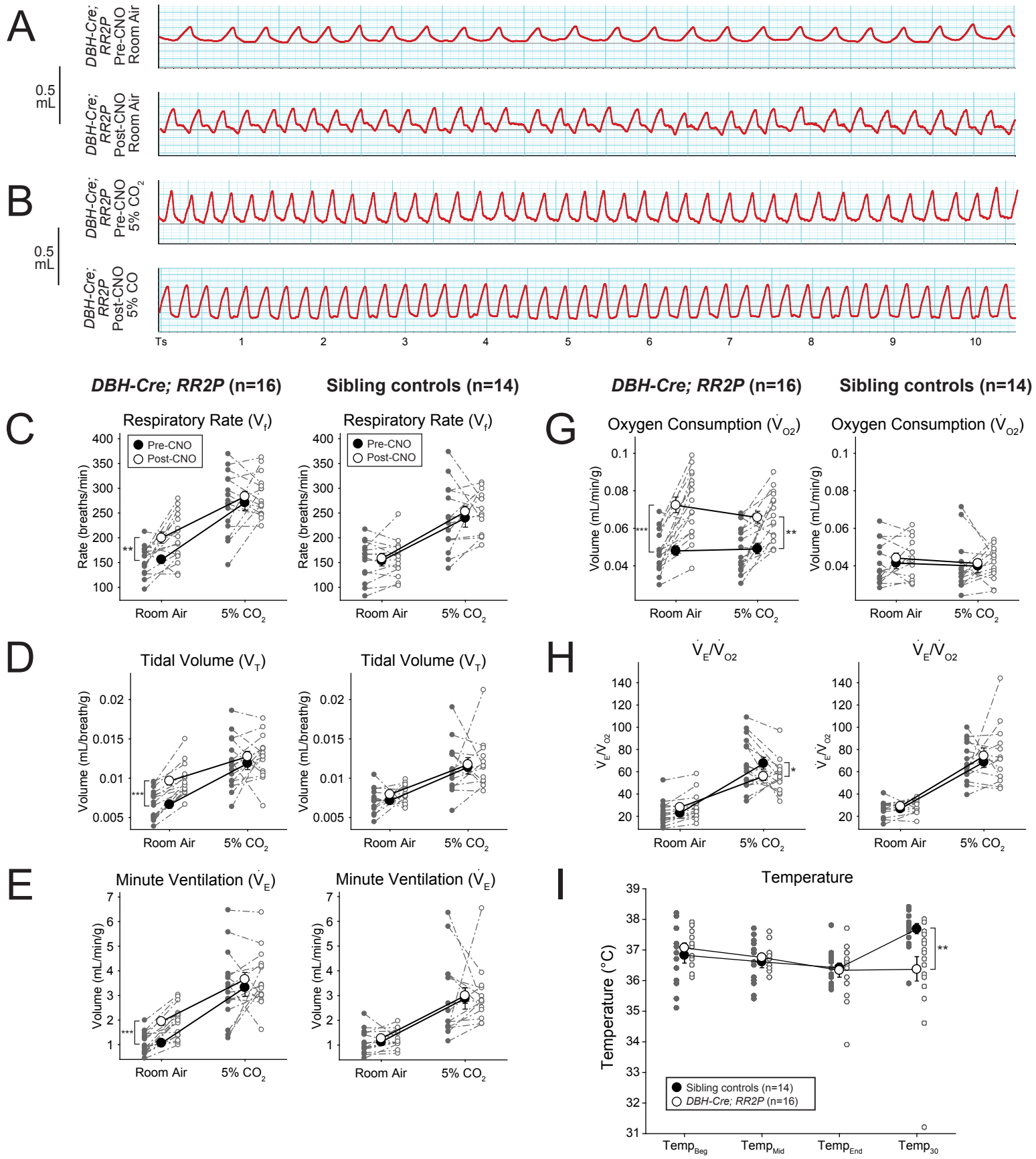
A
DBH-Cre; RR2P Pre-CNO Room Air
DBH-Cre; RR2P Post-CNO Room Air
0.5 mL
B
DBH-Cre; RR2P Pre-CNO 5% CO2
DBH-Cre; RR2P Post-CNO 5% CO
0.5 mL
Ts 1 2 3 4 5 6 7 8 9 10
DBH-Cre; RR2P (n=16)
Sibling controls (n=14)
C
Respiratory Rate (Vf)
Pre-CNO
Post-CNO
Rate (breaths/min)
Room Air
5% CO2
D
Tidal Volume (VT)
Volume (mL/breath/g)
E
Minute Ventilation (V̇E)
Volume (mL/min/g)
G
Oxygen Consumption (V̇O2)
Volume (mL/min/g)
H
V̇E/V̇O2
I
Temperature
Temperature (°C)
Sibling controls (n=14)
DBH-Cre; RR2P (n=16)
TempBeg
TempMid
TempEnd
Temp30

Figure 10

A

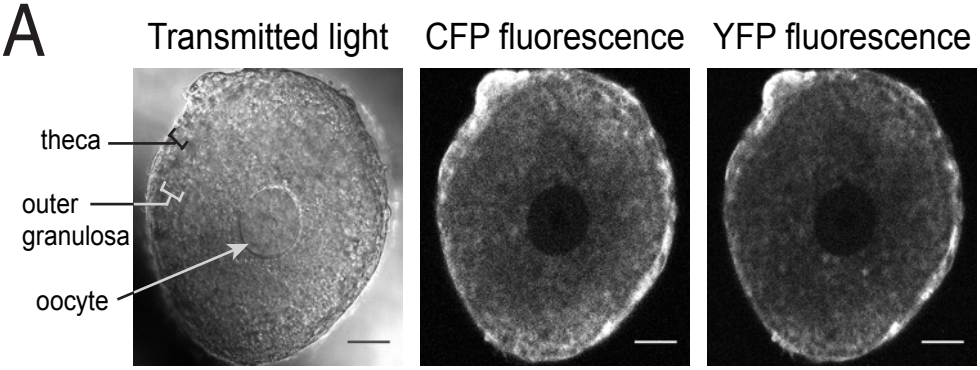
Transmitted light
CFP fluorescence
YFP fluorescence
theca
outer granulosa
oocyte

B

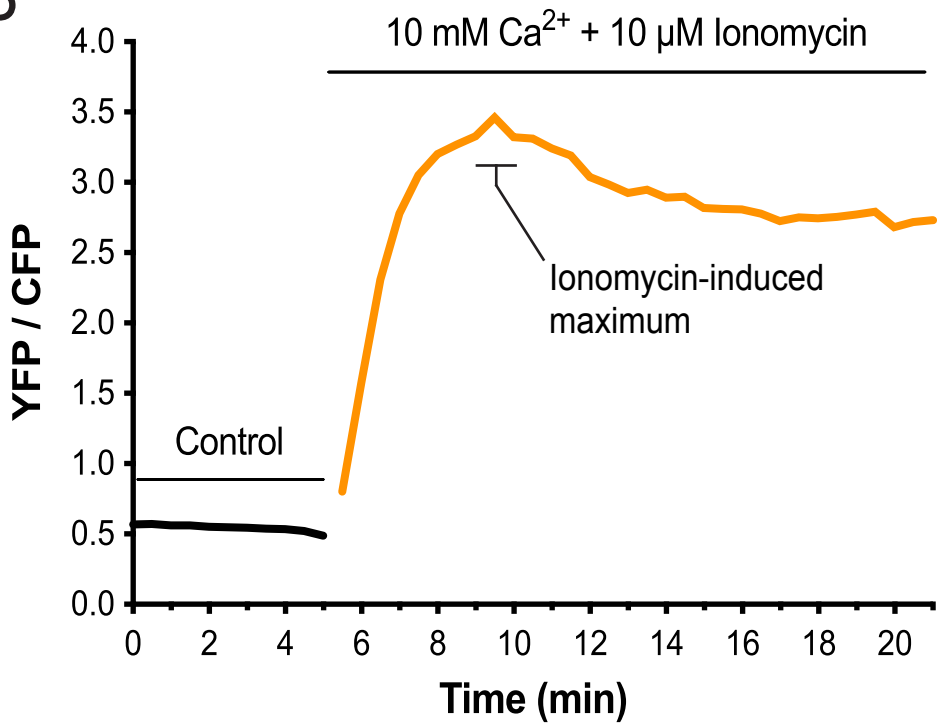
10 mM Ca2+ + 10 μM Ionomycin
Ionomycin-induced maximum
Control
YFP / CFP
Time (min)
4.0
3.5
3.0
2.5
2.0
1.5
1.0
0.5
0.0
0
2
4
6
8
10
12
14
16
18
20

Table 1

Vector	Function	Addgene ID Number
CAG Cas9 U6 Rosa26 sgRNA	Cas9 (px330) vector with sgRNA	97007
5' homology arm CAG F Neo S F P CS S CS P 3' homology arm	FLP and Cre responsive cloning vector	97012
5' homology arm CAG F S F P CS S CS P 3' homology arm	FLP and Cre responsive cloning vector (no neo)	99142
5' homology arm CAG P Neo S P CS 3' homology arm	Cre responsive cloning vector	97009
5' homology arm CAG F Neo S F CS 3' homology arm	FLP responsive cloning vector	97010
5' homology arm CAG R Neo S R CS 3' homology arm	Dre responsive cloning vector	97011
5' homology arm CS 3' homology arm	Empty *Rosa26* targeting vector	97008

*CS: Cloning site

Table 2

Short Name	MMRRC ID	Subtractive gene	Intersectional gene	Function	Line status
*RR1**	43516	*mCherry*	*hM4D*	Metabotropic neuron perturbation	Established and functional
Gt(ROSA)26Sor$^{tm\#(CAG\text{-}mCherry,\text{-}hM4D)Rray}$					
*RR2**	43515	*mCherry*	*hM3D*	Metabotropic neuron stimulation	Established and functional
Gt(ROSA)26Sor$^{tm\#(CAG\text{-}mCherry,\text{-}hM3D)Rray}$					
*RR3**	43518	*mCherry*	*EGFP-L10A*	Translating mRNA pulldown	Established
Gt(ROSA)26Sor$^{tm\#(CAG\text{-}mCherry,\text{-}EGFP\text{-}L10A)Rray}$					
*RR4**	43519	*mCherry*	*PSAM*	Ionotropic neuron perturbation	Established
Gt(ROSA)26Sor$^{tm\#(CAG\text{-}mCherry,\text{-}PSAM)Rray}$					
RR5	43513	None	*H2B-TagBFP; sfGFP; synaptophysin-tdTomato*	Intersectional fluorescent marking	Established and functional
Gt(ROSA)26Sor$^{tm\#(CAG\text{-}H2B\text{-}TagBFP\text{-}sfGFP\text{-}synaptophysin\text{-}tdTomato)Rray}$					
RR6	43517	*mCherry*	*Met-RS*	Synthesized protein pulldown	Established
Gt(ROSA)26Sor$^{tm\#(CAG\text{-}mCherry,\text{-}MetRS)Rray}$					
RR7	43514	*mCherry*	*Rs-EGFP*	Metabotropic Gs excitation	Established
Gt(ROSA)26Sor$^{tm\#(CAG\text{-}mCherry,\text{-}Rs\text{-}eGFP)Rray}$					
RR8	*TBD*	None	*Twitch2B*	Ratiometric calcium imaging	Established and functional
Gt(ROSA)26Sor$^{tm\#(CAG\text{-}Twitch2B)Rray}$					
RR9		*tdTomato*	*H2B-TagBFP; sfGFP*	Subtractive and intersectional fluorescent marking	Targeted ES cells
Gt(ROSA)26Sor$^{tm\#(CAG\text{-}tdTomato,\text{-}H2B\text{-}TagBFP\text{-}sfGFP)Rray}$					
RR10		None	*H2B-TagBFP; sfGFP*	Dre-responsive fluorescent marking	Targeted ES cells
Gt(ROSA)26Sor$^{tm\#(CAG\text{-}H2B\text{-}TagBFP\text{-}sfGFP)Rray}$					
RR11		None	*H2B-TagBFP; sfGFP; synaptophysin-tdTomato*	Dre-responsive fluorescent marking	Targeted ES cells
Gt(ROSA)26Sor$^{tm\#(CAG\text{-}H2B\text{-}TagBFP\text{-}sfGFP\text{-}synaptophysin\text{-}tdTomato)Rray}$					

Grey rows highlight Mouse Genome Informatics names; (tm#) are currently being determined
*Made using an earlier Rosa26 targeting vector without CRISPR/Cas9

Table 3

Knock-in Cassette	Short name	Length	Efficiency
CAG F S F P mCherry S P Met-RS	*RR6*	11037 bps	6/48 (13%)
CAG F S F P mCherry S P Rs-EGFP	*RR7*	9534 bps	1/48 (2%)
CAG F S F P tdTomato S P H2B-TagBFP sfGFP	*RR9*	9597 bps	6/48 (13%)
CAG R S R H2B-TagBFP sfGFP synaptophysin-tdTomato	*RR11*	9202 bps	5/48 (10%)
CAG R S R H2B-TagBFP sfGFP	*RR10*	6732 bps	9/48 (19%)
		Total	25/48 (52%)